Processing seismic ambient noise data to obtain reliable broad-band surface wave dispersion measurements

G.D. Bensen[1†], M.H. Ritzwoller[1], M.P. Barmin[1], A.L. Levshin[1], F. Lin[1], M.P. Moschetti[1], N.M. Shapiro[2], and Y. Yang[1],

1 - Center for Imaging the Earth's Interior, Department of Physics, University of Colorado at Boulder, Campus Box 390, Boulder, CO 80309, USA

2 - Laboratoire de Sismologie, CNRS, IPGP, 4 place Jussieu, 75252 Paris Cedex 05, France.

† To whom correspondence should be directed: gbensen@ciei.colorado.edu, 303-735-1850.

Resubmitted to *Geophysical Journal International*: January 24, 2007.

Abstract

Ambient noise tomography is a rapidly emerging field of seismological research. This paper presents the current status of ambient noise data processing as it has developed over the past several years and is intended to explain and justify this development through salient examples. The ambient noise data processing procedure divides into four principal phases: (1) single station data preparation, (2) cross-correlation and temporal stacking, (3) measurement of dispersion curves (performed with frequency-time analysis for both group and phase speeds), and (4) quality control, including error analysis and selection of the acceptable measurements. The procedures that are described herein have been designed not only to deliver reliable measurements, but to be flexible, applicable to a wide variety of observational settings, as well as being fully automated. For an automated data processing procedure, data quality control measures are particularly important to identify and reject bad measurements and compute quality assurance statistics for the accepted measurements. The principal metric on which to base a judgment of quality is stability, the robustness of the measurement to perturbations in the conditions under which it is obtained. Temporal repeatability, in particular, is a significant indicator of reliability and is elevated to a high position in our assessment, as we equate seasonal repeatability with measurement uncertainty. Proxy curves relating observed signal-to-noise ratios to average measurement uncertainties show promise to provide useful expected measurement error estimates in the absence of the long time series needed for temporal subsetting.

1. Introduction

Theoretical studies have shown that the cross-correlation of diffuse wavefields (e.g., ambient noise, scattered coda waves) can provide an estimate of the Green function between the stations (e.g., Weaver and Lobkis, 2001a, 2001b, 2004; Derode et al., 2003; Snieder, 2004; Wapenaar, 2004; Larose et al., 2005). Seismic observations based on cross-correlations between pairs of stations have confirmed the theory for surface waves using both coda waves (Campillo and Paul, 2003; Paul et al., 2005) and long ambient noise sequences (Shapiro and Campillo, 2004; Sabra et al., 2005a) and for crustal body waves using ambient noise (Roux et al., 2005). Oceanic applications are also feasible (Lin et al., 2006). An example of a year-long cross-correlation between a pair of Global Seismic Network (GSN) stations in the US filtered into several sub-bands is shown in Figure 1.

The first attempts to use ambient noise for surface wave tomography, called ambient noise surface wave tomography, were applied to stations in Southern California (Shapiro et al., 2005; Sabra et al., 2005b). These studies resulted in group speed maps at short periods (7.5 - 15 sec) that displayed a striking correlation with the principal geological units in California with low-speed anomalies corresponding to the major sedimentary basins and high-speed anomalies corresponding to the igneous cores of the main mountain ranges.

Ambient noise tomography is now expanding rapidly. Recent applications have arisen across all of California and the Pacific Northwest (Moschetti et al., 2007), in South Korea (Cho et al., 2006), in Tibet (Yao et al., 2006), in Europe (Yang et al., 2007), across New Zealand (Lin et al., 2007a), as well as elsewhere in the world. Most of the studies, to date, like the earlier work of Shapiro et al. (2005), have been performed in the microseism band below 20 sec period. Broad-band applications extending to considerably longer periods are now emerging (e.g., Bensen et al., 2005; Yao et al., 2006; Yang et al., 2007) and the method is also being applied to increasingly large areas such as Europe (Yang et al., 2007). In spite of these developments, the data processing procedures that underlie ambient noise tomography remain poorly documented, even as they have become increasingly refined. The purpose of this paper is to summarize the state of data processing as it has developed since the first papers on the

use of ambient noise to obtain surface wave dispersion measurements (Shapiro and Campillo, 2004).

In its current state, the ambient noise data processing procedure divides into four principal phases that are applied roughly in order: (1) single station data preparation, (2) cross-correlation and temporal stacking, (3) measurement of dispersion curves, and (4) quality control, including error analysis and selection of the acceptable measurements. These steps are presented schematically in Figure 2. After data processing is complete, tomography for group or phase speed maps (e.g., Yang et al., 2007) and inversion for a V_s model (e.g., Cho et al., 2006; Lin et al., 2007a) may follow, but discussion of these steps is beyond the scope of the present paper. The procedures in this paper are exclusively applied to Rayleigh waves, but Love wave studies have also begun to emerge (e.g., Cho et al., 2006).

In judging between candidate components of the data processing procedure, we have assigned significant weight to flexibility and the applicability to a wide variety of observational situations. The procedures described here, therefore, are designed to be applied over a broad range of periods, inter-station distances, and geographical scales. Examples are shown in this paper from regional to continental scales, from very short to long periods, and are drawn from Europe, North America, and New Zealand. Applications are, however, taken exclusively from continental or ocean island stations. Most are, in fact, taken from GSN stations within the US. As discussed by Lin et al. (2006), broad-band cross-correlations of ambient noise obtained at ocean bottom or sub-bottom seismometers (OBS) are contaminated at long periods (above $\sim$25 sec) by tilting under fluid flow and seafloor deformation under gravity waves. Crawford et al. (2006) argue that these effects can be mitigated on the vertical component using horizontal component data and a co-located differential seafloor pressure gauge. The success of this process will be needed for broad-band ambient noise measurements to be obtained from OBS data. We are unaware of research that has tested this idea in the context of ambient noise measurements, however.

Our principal purpose, therefore, is to summarize the status of the ambient noise data processing procedure that we have developed over the past several years. The paper is intended to explain, justify, and present salient examples of this development. It is also intended

to act as a primer to help provide guidance and act as a basis for future efforts in surface wave studies based on ambient seismic noise. Each of the four following sections presents a discussion of one phase of the data processing procedure, which ranges from processing data from a single station (section 2), cross-correlating and stacking data from station-pairs (section 3), measuring surface wave dispersion (section 4), and applying data quality control measures, particularly estimating uncertainties and selecting reliable measurements (section 5).

2. Single station data preparation

The first phase of data processing consists of preparing waveform data from each station individually. The purpose of this phase is to accentuate broad-band ambient noise by attempting to remove earthquake signals and instrumental irregularities that tend to obscure ambient noise. Obscuration by earthquakes is most severe above about 15 sec period, so this step of the data processing is most important at periods longer than the microseism band ($\sim$5 to $\sim$17 sec period). In addition, because the spectral amplitude of ambient noise peaks in the microseism band, methods have to be devised to extract the longer period ambient noise from seismic records. Figure 2 shows the steps that compose Phase 1 of data processing: removal of the instrument response, de-meaning, de-trending, and band-pass filtering the seismogram, time-domain normalization, and spectral whitening. This procedure is typically applied to a single day of data. Day data with less than 80% "on-time" are currently rejected, but this may be modified at the user's discretion. Some of the steps, such as the temporal normalization and spectral whitening, impose non-linear modifications to the waveforms, so the order of operations is significant. Because this phase of data processing is applied to single stations, rather than to station-pairs, it is much less time consuming and computationally intensive than subsequent cross-correlation, stacking, and measurement phases that are discussed in later sections of the paper. Our current applications involve from several dozen (e.g., 41 stations across New Zealand) to several hundred (e.g., 110 stations across Europe, $\sim$250 stations across North America) stations.

2.1 Temporal normalization

The most important step in single-station data preparation is what we call "time-domain" or "temporal normalization". Time-domain normalization is a procedure for reducing the effect on the cross-correlations of earthquakes, instrumental irregularities, and non-stationary noise sources near to stations. Earthquakes are among the most significant impediments to automated data processing. They occur irregularly and, although the approximate times and locations of large earthquakes can be found in earthquake catalogs, small earthquakes over much of the globe are missing from global catalogs. In addition, the time of arrival of surface wave phases at short periods is not well known. Thus, removal of earthquake signals must be data-adaptive, rather than prescribed from a catalog.

We have considered five different methods to identify and remove earthquakes and other contaminants automatically from seismic waveform data. An illustrative example is shown in Figure 3. The first and most aggressive method is called "one-bit" normalization (Figure 3b), which retains only the sign of the raw signal by replacing all positive amplitudes with a 1 and all negative amplitudes with a -1. This method has been shown to increase signal-to-noise ratio (SNR) when employed in acoustic experiments in the laboratory (Larose, et al. 2004) and has been used in a number of early seismic studies of coda waves and ambient noise (Campillo and Paul, 2003, Shapiro and Campillo 2004, Shapiro et al., 2005; Yao et al. 2006). The second method, employed for example by Sabra et al. (2005a), involves the application of a clipping threshold equal to the root-mean-square (rms) amplitude of the signal for the given day. An example is shown in Figure 3c. The third method, illustrated by Figure 3d, involves automated event detection and removal in which 30 minutes of the waveform are set to zero if the amplitude of the waveform is above a critical threshold. This threshold is arbitrary and its choice is made difficult by varying amplitudes at different stations. The fourth method is running-absolute-mean normalization, which is the method of time normalization that we promote here. This method computes the running average of the absolute value of the waveform in a normalization time window of fixed length and weights the waveform at the center of the window by the inverse of this average. That is, given a discrete time-series d_j, we

compute the normalization weight for time point n as:

$$w_n = \frac{1}{2N+1} \sum_{j=n-N}^{n+N} |dj| \tag{1}$$

so that the normalized datum becomes $\tilde{d}_n = d_n / w_n$. The width of the normalization window $(2N + 1)$ determines how much amplitude information is retained. A one-sample window $(N = 0)$ is equivalent to one-bit normalization, while a very long window will approach a re-scaled original signal as $N \to \infty$. After testing various time window widths, we find that about half the maximum period of the pass-band filter works well and that this length can be varied considerably and still produce similar results. An example result of the application of this method is shown in Figure 3e. This method is not without its faults, however. For example, it does not surgically remove narrow data glitches, as it will inevitably down-weight a broad time-interval around the glitch. One-bit normalization does not suffer from this shortcoming. Finally, there is a method that we call iterative "water-level" normalization in which any amplitude above a specified multiple of the daily rms-amplitude is down-weighted. The method is run repeatedly until the entire waveform is below the water-level, which is six times the daily rms level in the example shown in Figure 3f. This method of time-domain normalization is the most time-intensive of the candidates considered here.

Figure 4 presents examples of year-long cross-correlations, band-pass filtered between 20 sec and 100 sec period, using each of these methods of time-domain normalization. The raw data (Fig. 4a), the clipped waveform method (Fig. 4c), and the automated event detection method (Fig. 4d) produce noisy cross-correlations in this period band. The one-bit normalization (Fig. 4b), the running-absolute-mean normalization (Fig. 4e), and the water-level normalization (Fig. 4f) methods produce relatively high signal-to-noise ratio (SNR) waveforms displaying signals that arrive at nearly the same time. In this example, the one-bit and the running-absolute-mean normalizations are nearly identical. A systematic test has been performed using 15 GSN stations in North America using the observed spectral SNR (defined in section 3) at 20 sec period to compare the methods at five periods. The resulting SNR values are similar for one-bit normalization and the running-absolute-mean normalization. The water-level normalization method also allows meaningful results to be

recovered. The running-absolute-mean method provides a small enhancement to SNR values above one-bit normalization at all periods and a more significant improvement over the water-level normalization.

The principal reason we prefer running-absolute-mean normalization over the water-level or one-bit normalization methods is its greater flexibility and adaptability to the data. For example, in areas with high regional seismicity it is desirable to tune the time-domain normalization to the frequency content of the seismicity. Figure 5 shows that if the temporal weights of the running-absolute-mean normalization are computed on the raw waveform data, small earthquakes can get through the procedure because they exist in the raw waveform near the background noise level. Earthquakes are revealed by a low-pass filter both in the raw waveform (Fig. 5b) and the temporally normalized waveform (Fig. 5d). Alternately, the temporal weights of the running-absolute-mean normalization can be computed on the waveform filtered in the earthquake band (Fig. 5b). In this case, if d_j is the raw seismogram and $\hat{d}_j$ is the seismogram band-pass filtered in the earthquake band, we define new temporal weights calibrated to the regional seismicity

$$\hat{w}_n = \frac{1}{2N+1} \sum_{j=n-N}^{n+N} |\hat{dj}|. \tag{2}$$

These weights are then applied to the raw data as before ($\tilde{d}_n = d_n/\hat{w}_n$). This procedure severely down-weights time-series during earthquakes (Fig. 5e), which more effectively removes them from low-pass filtered seismograms (Fig. 5f). Contamination by earthquakes of the cross-correlations, therefore, should be ameliorated.

Earthquake signals that pass through the temporal normalization tend to appear on cross-correlations as spurious precursory arrivals, such as the high amplitude arrivals appearing between 0 - 100 sec in the 12-month cross-correlation shown in Figure 6a. Defining the temporal normalization weights in the earthquake band, however, reduces the amplitude of the precursors, as Figure 6b illustrates. This process will be most important in regions with significant regional seismicity. The example shown in Figure 6 is from New Zealand where, because of high levels of seismicity in the Fiji and Tonga-Kermadec regions, the process is recommended strongly (Lin et al., 2007a).

2.2 Spectral normalization or whitening

Ambient noise is not flat in the frequency domain (i.e., is not spectrally white), but is peaked near the primary (around 15 sec period) and secondary (around 7.5 sec period) microseisms and rises at very long periods above 50 sec to form a signal now referred to as Earth "hum" (e.g., Rhie and Romanowicz, 2004). Figure 7a presents an example of an amplitude spectrum for a day long time series obtained after temporal normalization. Primary and secondary microseisms as well as Earth hum signatures can be seen clearly on this record which was band-pass filtered between 7 sec and 150 sec period. In addition to these signals, there is a smaller peak near 26 sec that is caused by a persistent narrow-band noise source in the Gulf of Guinea (Shapiro et al., 2006). Without the temporal normalization, which reduces the effect of earthquakes, the 26 sec resonance typically is not seen. Ambient noise is minimum in the period range from about 30-70 sec. Inversely weighting the complex spectrum by a smoothed version of the amplitude spectrum produces the normalized or whitened spectrum shown in Figure 7b. Spectral normalization acts to broaden the band of the ambient noise signal in cross-correlations and also combats degradation caused by persistent monochromatic sources such as the Gulf of Guinea source.

First, regarding the problem of an isolated, persistent nearly monochromatic noise source, the grey box in Figure 7a highlights the noise peak at 26 sec period as observed at the station HRV on a northern summer day. As documented by Holcomb (1998), this signal is seasonal, being much stronger in the northern summer than in the winter. Figure 8a shows a 12-month cross-correlation between GSN stations ANMO and CCM in which spectral normalization has not been applied. The 26 sec resonance appears as a broad envelope in the time domain and corrupts the cross-correlation at positive correlation lag. Shapiro et al. (2006) used the apparent arrival time of the 26 sec signal observed at stations in North America, Europe, Africa, and Asia to locate the source in the Gulf of Guinea. The amplitude spectrum of this cross-correlation displays the prominent peak at ∼26 sec period (∼0.038 Hz) as seen in Figure 8b. In contrast, Figures 8c and 8d show the cross-correlation and its amplitude spectrum where spectral normalization has been applied. The effect of the 26 sec resonance is greatly

reduced. Shapiro et at. (2006) recommend eradicating this problem by applying a narrow band reject filter centered around 26 sec period. Figures 8e and 8f show the effect of this filter. The cross-correlation is largely unchanged compared to spectral whitening. In many cases, therefore, the more gentle approach of spectral whitening is sufficient to eliminate the 26 sec problem from the cross-correlations. The band-reject filter also creates problems for automated dispersion measurement in a later stage of processing, so spectral whitening is preferable if it suffices to ameliorate the effect of the 26 sec microseism.

Second, spectral normalization seeks to reduce broad imbalances in single-station spectra to aid in the production of a broad-band dispersion measurement. Figures 9a and 9b show a one-month broad-band cross-correlation between stations CCM (Cathedral Cave, MO, USA) and SSPA (Standing Stone, PA, USA) for spectrally un-whitened and whitened data taken during the northern spring (when the 26 sec resonance is weak). Figures 9c and 9d display the amplitude spectra of the un-whitened and whitened cross-correlations, respectively. Without the whitening, Figure 9c shows that the resulting cross-correlation is dominated by signals in the microseism band, predominantly from 15 to 17 sec and from 6 to 9 sec period. Not surprisingly, spectral whitening produces a broader-band signal. In many cases, the cross-correlation amplitude spectrum is shaped with the longer periods having higher amplitudes than the shorter periods, as in Figure 9d. This is apparently because the longer period ambient noise, although naturally lower in amplitude than microseismic noise, propagates more coherently over long distances. Additional whitening of the cross-correlation prior to dispersion measurement is an added option.

3. Cross-correlation, stacking, and signal emergence

After the preparation of the daily time-series described in section 2, the next step in the data processing scheme (Phase 2) is cross-correlation and stacking. Although some inter-station distances may be either too short or too long to obtain reliable measurements, we perform cross-correlations between all possible station pairs and perform data selection later. This yields a total of $n(n-1)/2$ possible station pairs, where n is the number of stations. Obtaining tens of thousands of cross-correlations is common when ambient noise

data processing is performed over large spatial scales such as Europe (e.g., Yang et al., 2007) or North America (e.g., Bensen et al., 2005).

Cross-correlation is performed daily in the frequency domain. After the daily cross-correlations are returned to the time-domain they are added to one another, or "stacked", to correspond to longer time series. Alternately, stacking can be done in the frequency domain which would save the inverse transform. We prefer the organization that emerges from having daily raw time-series and cross-correlations that are then stacked further into weekly, monthly, yearly, etc. time-series. In any event, the linearity of the cross-correlation procedure guarantees that this method will produce the same result as cross-correlation applied to the longer time series. The resulting cross-correlations are two-sided time functions with both positive and negative time coordinates, i.e., both positive and negative correlation lags. We typically store the correlations from -5000 to 5000 sec, but the length of the time series needed will depend on the group speeds of the waves and the longest inter-station distance.

The positive lag part of the cross-correlation is sometimes called the "causal" signal and the negative lag part the "acausal" signal. These waveforms represent waves traveling in opposite directions between the stations. Several examples of cross-correlations have been shown earlier in the paper. Figures 4, 8, and 9 display some two-sided cross-correlations for different time-series lengths. Figure 1 clearly shows the broad-band content of ambient noise. If sources of ambient noise are distributed homogeneously in azimuth, the causal and acausal signals would be identical. However, considerable asymmetry in amplitude and spectral content is typically observed, which indicates differences in both the source process and distance to the source in the directions radially away from the stations. We often compress the two-sided signal into a one-sided signal by averaging the causal and acausal parts. We call this the "symmetric" signal or component. An example was shown in Figures 1 and 6.

Stacking over increasingly long time-series, on average, improves signal-to-noise ratio. An example is shown in Figure 10, which displays cross-correlations of different length time-series from the stations ANMO and DWPF (Disney Wilderness Preserve, FL, USA). The causal and acausal signals are seen to emerge as the time-series length increases in both of the period bands that are displayed in Figures 10a and 10b.

Measurements of the frequency dependence of the SNR are useful to quantify observations of the emergence of the signals with increasing time-series length. We also use it as part of data selection in Phase 4 of the data processing procedure. Figure 11 illustrates one way in which the frequency dependence of SNR may be measured. From the 3-D model of Shapiro and Ritzwoller (2002), we predict the maximum and minimum group arrival times (t_{min}, t_{max}) expected for the path between the station-pair over the period band of interest (τ_{min}, τ_{max}). We perform a series of narrow band-pass filters centered on a discrete grid of frequencies and measure the peak in the time domain in a signal window $(t_{min} - \tau_{max}, t_{max} + 2\tau_{max})$ shown with solid vertical lines in Figure 11. We also measure the root-mean-square (rms) noise level in a 500 sec noise window (vertical dashed lines) that trails the end of the signal window by 500 sec. This rms level is shown with dotted lines in Figure 11 in the noise window. The resulting ratio of peak signal in the signal window to rms noise in the trailing noise window on the grid of center frequencies is the "spectral" SNR measurement. Center periods and SNR are identified in each panel of Figure 11. Note that although we call this a spectral SNR measurement, it is, in fact, a measurement of SNR in the time-domain. It is "spectral" only in the sense that the measurements are a function of frequency.

This spectral SNR, which takes the ratio of signal to trailing noise, mostly is a measure of the signal level, as the trailing noise does not strongly depend on signal-generated noise. Alternately, one could define the ratio of signal to leading noise, which is strongly dependent on signal-generated noise, as discussed earlier. Although we do not use signal-to-precursory-noise here, it has the advantage of quantifying precursory noise which interferes with dispersion measurements more than trailing noise. Further research is needed to determine if it is a better predictor of the quality of dispersion measurements than the spectral SNR that we use.

A spectral SNR curve for the 24-month cross-correlations between stations ANMO and DWPF, shown in Figure 10a and 10b, is presented as the dashed line in Figure 10c. It is contrasted with the average SNR over all GSN station pairs within the US. For this example, spectral SNR, on average, peaks in the primary microseism band around 15 sec period, minimizes near 40 sec period, and then is fairly flat to much longer periods, although it rises slightly. The details of the curve, however, will vary geographically, with path length, and

season. Figure 10d shows how spectral SNR increases with time-series length. The shapes of the SNR spectra also change subtly with time-series length.

In general, therefore, as time-series length increases so does SNR, so the longer the time-series the better. The details of how the signal emerges from noise depends on frequency, and also on the location and inter-station spacing. Figure 12 presents an example of how SNR depends on time-series length computed for the 15 GSN stations in the US. The emergence of the signal can be fit well with a power law, and Figure 12 shows the fit power law rather than the raw data: SNR $= At^{1/n}$, where A and n are period dependent. For the periods shown in Figure 12, n varies from about 2.55 at 10 sec period to 2.88 at 25 sec. It attains a maximum of about 3.4 at 50 sec and then diminishes again so that at 100 sec period n is about equal to 2.66. Inspection of Figure 7, which is a typical daily amplitude spectrum for temporally normalized data, reveals that n maximizes at intermediate periods between about 25 and 50 sec where ambient noise is generally weakest. In this period band, the emergence of the signal is slowest. At shorter and longer periods, in the microseismic and "Earth-hum" bands, n ranges from about 2.5 to 2.9, and the signal emerges at a faster rate than at the intermediate periods. As discussed in section 6 below, the curves in Figure 12 are useful in designing experiments based on ambient noise tomography. Further work, however, is needed to understand the frequency dependence of the power law behavior of the emergence of the signal from ambient noise, as well as its geographic variability.

4. Dispersion measurement

After the daily cross-correlations have been computed and stacked, the resulting waveform is an estimated Green function. Using the estimated Green function, the group and phase speeds as a function of period can be measured by using traditional frequency-time analysis (FTAN) (e.g., Dziewonski et al., 1969; Levshin et al., 1972, 1992; Herrin and Goforth, 1977; Russell et al., 1988; Levshin et al., 1989; Ritzwoller and Levshin, 1998; Levshin and Ritzwoller, 2001). This is Phase 3 of the data processing procedure. As with Phases 1 and 2, because the number of inter-station pairs can be very large, the dispersion measurement process needs to be automated. The method that we promote is based on a version of FTAN described

in detail by Levshin et al. (1989), which obtains measurements on single waveforms and involves significant analyst interaction. However, the computational structure of FTAN allows automation and this is what we describe here. Although FTAN has been applied dominantly to measure group speeds, phase speed curves are also measured naturally in the process.

We roughly follow the notation and terminology of Bracewell (1978), but if $s(t)$ is the waveform of interest its Fourier transform is defined with a positive exponent as $S(\omega) = \int_{-\infty}^{\infty} s(t) \exp(i\omega t) dt$. Dispersion measurements are obtained by considering the "analytic signal", which is defined simply in the frequency domain as

$$S_a(\omega) \quad = \quad S(\omega) \left(1 + \mathrm{sgn}(\omega)\right), \tag{3}$$

and upon inverse Fourier transforming is expressed in the time domain as follows:

$$S_a(t) \quad = \quad s(t) + iH(t) = |A(t)| \exp(i\phi(t)). \tag{4}$$

$H(t)$ is the Hilbert transform of $s(t)$. To construct a frequency - time function, the analytic signal is subjected to a set of narrow band-pass Gaussian filters with center frequencies ω_0:

$$S_a(\omega, \omega_0) \quad = \quad S(\omega) \left(1 + \mathrm{sgn}(\omega)\right) G(\omega - \omega_0), \tag{5}$$

$$G(\omega - \omega_0) \quad = \quad e^{-\alpha \left(\frac{\omega - \omega_0}{\omega_0} \right)^2} \tag{6}$$

Inverse transforming each band-passed function back to the time domain yields the smooth 2D envelope function, $|A(t, \omega_0)|$, and phase function, $\phi(t, \omega_0)$. α is a tunable parameter that defines the complementary resolutions in the frequency and time domains and is commonly made distance dependent (Levshin et al., 1989). Group speed is measured using $|A(t, \omega_0)|$ and phase speed using $\phi(t, \omega_0)$. In particular, the group arrival time, $\tau(\omega_0)$, as a function of the center frequency of the Gaussian filter is determined from the peak of the envelope function so that the group speed is $U(\omega_0) = r/\tau(\omega_0)$, where r is the inter-station distance. We follow Bracewell and replace ω_0 with the "instantaneous frequency", defined as the time rate of change of the phase of the analytic signal at time τ. We, therefore, replace the center frequency of the narrow-band filter, ω_0, with the instantaneous frequency, $\omega = |d\phi(t, \omega_0)/dt|_{t=\tau(\omega_0)}$. This correction is most significant when the spectrum of the input waveform is not flat, in

which case, due to spectral leakage, the central frequencies of the narrow-band filters will not accurately represent the frequency content of the output of the filters.

The measurement of dispersion curves divides into eight steps. We discuss each step and then indicate how the analyst-driven and the automated FTAN processes differ. This will be done in the context of group velocity measurements in section 4.1 and then we will follow with a discussion of how FTAN measures phase speed curves in section 4.2. Figure 13 graphically illustrates the process. In this figure, all results are for the automated FTAN process.

4.1 Group speed measurements

Figure 13a shows a broadband signal obtained from a one-year cross-correlation between stations ANMO and COR in the US. In Step 1 of FTAN, a frequency (period) - time (group speed) or FTAN image is produced by displaying the logarithm of the square of the envelope of the analytic signal, $\log |A(t, \omega_0)|^2$. Figure 13b shows the FTAN image of the waveform in Figure 13a. The envelope functions $\log |A(t, \omega_0)|^2$ are arrayed vertically on a grid of different values of ω_0 to produce a matrix that can be displayed as a 2-D image. There is a similar phase matrix not displayed here. Typically, group speed replaces time and period replaces filter center frequency. In Step 2, the dispersion ridge is tracked as a function of period to obtain a raw group speed curve. Figure 13b shows this curve and the prediction from the 3-D model of Shapiro and Ritzwoller (2002). This raw group speed measurement may be sufficient for many applications.

Steps 3-8 of FTAN involve phase-matched filtering to clean the waveform of potential contamination and generate an alternative group speed curve. This measurement may be preferable in some applications. In Step 3, an anti-dispersion or phase-matched filter is defined on a chosen period-band. Levshin and Ritzwoller (2001) discuss the phase-matched filtering method in detail. In Step 4, this anti-dispersion filter is applied to the waveform in the period band chosen to produce the undispersed signal. Figure 13c shows the undispersed or "collapsed" signal. In Step 5, contaminating noise is identified and removed from the undispersed signal. Typically, for earthquakes this noise is signal-generated, being composed of multi-pathed signals, seismic coda, body waves, and so forth. An example cut is shown

with the red line in Figure 13c. In Step 6, the cleaned collapsed waveform is redispersed. It is shown as the red line in Figure 13a. In Step 7, the FTAN image of the cleaned waveform is computed using the same process applied to the raw waveform in Step 1. Figure 13d shows the FTAN image of the cleaned waveform. To improve frequency resolution, the Gaussian filters that are applied during phase-matched filtering are broader than those that are applied to the raw waveform. For this reason, the time-width of the FTAN image is broader in Figure 13d than in Figure 13b, but this does not reflect a lower intrinsic temporal resolution because interfering signals have been removed. Finally, in Step 8, the dispersion ridge is tracked as a function of period on the cleaned FTAN image to obtain the cleaned group speed curve. Figure 13d shows this curve and the predicted curve from the 3-D model.

The traditional analyst-driven FTAN procedure has been applied to earthquake data by analysts for more than 200,000 individual paths globally (e.g., Shapiro and Ritzwoller, 2002). The analyst, however, only enters the process in Steps 3 and 5. In Step 3, the analyst defines the phase-matched filter and the frequency band of interest, which usually depends on the band-width of the signal that is observed. The analyst either can use the group speed curve that is automatically produced on the raw FTAN image in Step 2 or can define a curve interactively. The latter approach is usually chosen, as FTAN images of earthquake data commonly display spectral holes that vitiate the automated group speed measurement. The automated group speed measurements are also often tricked by scattered or multipathed arrivals and, therefore, do not track the dispersion branch of interest accurately. Multipathing and scattering is a problem mostly for large epicentral distances. In Step 5, the analyst interacts with the collapsed signal to remove noise. It is, therefore, only Steps 3 and 5 that require automation beyond the existing method.

To automate Step 3, the group speed measurements that result in Step 2 must be used to define the phase-matched filter. Therefore, these measurements must be robust to spectral holes and scattered or multipathed arrivals. Fortunately, high SNR FTAN images that result from cross-correlations of ambient noise tend to be much simpler than those from earthquakes, and spectral holes are rare. Inter-station spacings for ambient noise measurements are also typically shorter than epicentral distances, so multipathing is not as severe of a problem. The

automated procedure, therefore, only differs from the raw group velocity procedure applied during interactive FTAN in that in Step 2 added measures are taken to ensure the continuity of the dispersion curve by rejecting spurious glitches or jumps in group times. Formal criteria are set to reject curves with distinctly irregular behavior or to interpolate through small glitches by selecting realistic local instead of absolute maxima. When gaps or jumps are too large in amplitude or persistent in period, the dispersion curve is rejected. Spectral whitening (section 2.2) helps to minimize jumps in the measured curve as well as the incompleteness of measurements at the long period end of the spectrum. The raw group speed curve that emerges from Step 2 is one of two alternative curves that emerge from the automated process.

To automate Step 5, the undispersed signal is selected from the surrounding noise automatically. Figure 13c illustrates this procedure graphically using the waveform from Figure 13a. In an ideal case, the anti-dispersed signal will collapse into a single narrow spike. The collapsed waveform, given by the red line in Figure 13c, is then cut from the surrounding time-series and re-dispersed to give the clean waveform shown with the red line in Figure 13a. In this example the collapsed waveform is more complicated than a single spike. The principal advantage of this phase-matched filtering method arises when there exists strong neighboring noise that can be removed from the undispersed signal. In the case of ambient noise cross-correlations, spurious precursory arrivals exist in many cases, particularly at long periods. A good example can be seen in Figure 6a, and the example in Figure 13a also contains precursory arrivals. Such arrivals tend to interfere with the primary signals and can make the resulting group velocity curves undulatory. Phase-matched filtering helps to reduce the effect of precursory arrivals and smooths the measured group speed curve in general. The FTAN image after phase-matched filtering is broader in time (Fig. 13d) because a larger α -value (eqn 6) is applied compared to the raw image (Fig. 13b) In the example in Figure 13, however, there is little difference between the group speed curves that emerge from the raw and phase-match filtered FTAN images.

A problem occurs with phase-matched filtering, however, when the waveform of interest is narrow-band. In this case, the undispersed signal will possess prominent side-lobes that will need to be included in the cleaned collapsed signal cut from surrounding noise. If these

side-lobes extend broadly enough in time, the cutting procedure may not effectively eliminate contaminating noise. Alternately, if the side-lobes are not included in the selected waveform, the redispersed signal will be biased and the dispersion curve will often be undulatory at the long period end of the measurement. For these reasons, phase-matched filtering (i.e., FTAN Steps 3-8) is only recommended for application to broad-band signals.

4.2 Phase speed measurements

By analyzing the envelope function, $|A(t,\omega)|$, the group speed curve, $U(\omega)$, is measured. Phase speed cannot be derived directly from group speed, but the group speed can be computed from phase speed. To see this, let $U = \partial\omega/\partial k$ and $c = \omega/k$ be group and phase speed, respectively, $s_u = U^{-1}$ and $s_c = c^{-1}$ be group and phase slowness, respectively, and k be wavenumber. Then $s_u = \partial k/\partial\omega = \partial(\omega s_c)/\partial\omega$, which gives the following first-order differential equation relating the group and phase slownesses at frequency ω:

$$\frac{\partial s_c}{\partial \omega} + \omega^{-1} s_c = \omega^{-1} s_u. \tag{7}$$

If the phase speed curve $c(\omega)$ is known, the group speed curve $U(\omega)$ can be found directly from this equation. If the group speed curve is known, this differential equation must be solved to find $c(\omega)$, which involves an integration constant that is generally unknown. The solution is

$$s_c(\omega) = \omega^{-1} \left(\int_{\omega_n}^{\omega} s_u(\omega) d\omega + \omega_n s_c^n \right), \tag{8}$$

where the constant of integration has been written in terms of a boundary condition that the phase speed curve is known at some frequency ω_n: $s_c(\omega_n) = s_c^n$. This is a condition that will generally not apply. Nevertheless, knowledge of the group speed can help to find the phase speed, as we now show.

Measurement of the phase speed curve requires information in addition to the envelope function on which the group speed has been measured. This information derives from the phase of the analytic signal which is approximately composed of a propagation term, an initial source phase, and a phase ambiguity term that will be discussed further below. At instantaneous frequency ω, this can be written:

$$\phi(t,\omega) = k\Delta - \omega t - \phi_s - \phi_a, \tag{9}$$

where t is the travel time, Δ is distance (inter-station or epicentral), k is wavenumber, ϕ_s is source phase, and ϕ_a is the phase ambiguity term. To proceed, we evaluate the observed phase at the observed group arrival time, $t_u = \Delta/U$, and let $k = \omega s_c$ to find the expression for phase slowness:

$$s_c = s_u + (\omega\Delta)^{-1} \left(\phi(t_u) + \phi_s + \phi_a\right). \tag{10}$$

where we now suppress the ω notation for simplicity. The group speed curves, therefore, enter this process by defining the point in time at which the observed phase is evaluated.

Equation (10) prescribes the phase slowness (and hence the phase speed) curve. Its use, however, depends on knowledge of the initial source phase and the extra phase ambiguity term. In earthquake seismology, ϕ_s is typically computed from Centroid Moment Tensor (CMT) solutions. One of the traditional advantages of studies of group speed over phase speed is that source phase plays a secondary role in group speed (Levshin et al., 1999), particularly at short periods. Group speeds, therefore, can be measured at short periods unambiguously using small earthquakes without prior knowledge of the CMT solution. For cross-correlations of ambient noise, however, the situation is considerably easier, as the source phase should be zero: $\phi_s = 0$.

For both earthquake and ambient noise studies, the phase ambiguity term contains a part derived from the 2π ambiguity inherent to any phase spectrum: $\phi_a = 2\pi N$, where $N = 0, \pm1, \pm2, \ldots$. Typically, this ambiguity can be resolved by using a global 3-D model (e.g., Shapiro and Ritzwoller, 2002) or phase velocity maps (e.g., Trampert and Woodhouse, 1995; Ekstrom et al., 1997) to predict phase speed at long periods. The value of N then is chosen to give the closest relation between these predictions and observation. If observations extend to long periods (e.g., greater than 40 sec, preferably longer), a global model or observed phase velocity maps may predict phase speed well enough to get N right in most cases. As discussed in section 5, we recommend making dispersion measurements only up to a period (in sec) equal to $\Delta/12$, where Δ is in km. To obtain a 40 sec measurement, therefore, requires an inter-station spacing of about 500 km. If resolution of the phase ambiguity requires 100 sec observations, then an inter-station spacing of at least 1200 km is recommended. For ambient noise cross-correlations, if observations are limited to short periods or short inter-station

distances, the phase ambiguity may not resolve in a straightforward way.

For ambient noise cross-correlations, the phase ambiguity appears to be exacerbated by another factor. Equation (23) of Snieder (2004) shows that the phase of the cross-correlation between displacement waveforms possesses a $\pi/4$ term that arises from the stationary phase integration (effectively over sources) in the direction transverse to the two stations. The sign of the term depends on the component of the seismometer, positive for the vertical component and negative for the radial component for a Rayleigh wave. The assumption, however, is that sources are homogeneously distributed with azimuth. An inhomogeneous distribution may produce a different phase shift and, because this distribution may vary with frequency, the shift could be frequency dependent. More theoretical work is needed on this problem, but an empirical argument made by Lin et al. (2007b) demonstrates that for velocity waveforms the value appears to be $-\pi/4$ for the vertical component. Thus, following Lin et al. (2007b) for vertical component ambient noise cross-correlations between velocity waveforms the phase ambiguity term is $\phi_a = 2\pi N - \pi/4$.

In summary, phase-slowness derived from a vertical component ambient noise cross-correlation can be written

$$s_c = s_u + (\omega\Delta)^{-1} \left(\phi(t_u) + 2\pi N - \pi/4\right). \tag{11}$$

where $N = 0, \pm 1, \pm 2, \ldots$. More theoretical work and simulations are needed to determine the uncertainty in the $-\pi/4$ phase shift as well as the possible dependence on frequency and geographical location.

5. Quality control

Because the number of inter-station paths grows as the square of the number of stations, the data processing procedure that is applied to ambient noise cross-correlations must be designed to require minimal human interaction. Erroneous dispersion measurements are more likely to arise than if analysts were providing guidance at strategic intervals along the process. Data quality control measures, therefore, must be devised to identify and reject bad measurements and compute quality assurance statistics for the accepted measurements.

First, we have found that a reliable dispersion measurement at period τ requires an inter-station spacing (Δ in km) of at least 3 wavelengths (λ): $\Delta > 3\lambda = 3c\tau$ or $\tau < \Delta/3c$. Because phase speed $c \sim 4$ km/sec, for measurements obtained at an inter-station spacing of Δ, there is a maximum cut-off period of about $\tau_{\max} = \Delta/12$. We clearly observe the degradation of dispersion measurements at periods greater than about $\tau_{\max}$, at least for group speeds. This imposes a severe constraint on measurements obtained from small regional arrays such as PASSCAL experiments. A broad-band network 500 km in extent, for example, can only produce measurements up to about 40 sec period, and that only for the stations across the entire array which is a small subset of the inter-station paths. Intermediate and long period measurements most likely will be obtained from the array to surrounding stations, which indicates the importance of permanent (back-bone) stations in the context of regional deployments. At present, we have less experience with phase speed measurements obtained on cross-correlations of ambient noise, so it is possible that the period cut-off may be able to be relaxed for phase speeds.

Second, we need the means to determine the reliability of dispersion measurements that satisfy the period cut-off criterion. One way to estimate reliability is comparison with ground truth. The best case would be when an earthquake has occurred beneath one of the stations. Figures 14 and 15 present an example comparison, using an earthquake that occurred near station PFO (Pinyon Flat, CA, USA). (Date = Oct 31, 2001, m_b = 5.2, lat = 33.508, lon = -116.514, depth = 15.2 km). The five paths that are selected are shown in Figure 14 and comparison between the cross-correlation and the earthquake signals is presented in Figure 15. To limit the comparison to the period range where both signals are strong, we multiplied the earthquake amplitude spectrum by the cross-correlation amplitude spectrum. This was then used as the amplitude spectrum for both signals. In general, the arrival times of the fundamental Rayleigh waves (the largest amplitude arrivals in each panel) are similar, particularly in light of the source phase shift that affects the earthquake. To compensate for the earthquake radiation pattern, we flip the sign of the earthquake records for stations CMB (Columbia, CA, USA) and LLLB (Lillooet, BC, Canada) which are to the north of station PFO. Also, because the earthquake is south-west of station PFO, the epicentral distances to

the stations are greater than the distance between PFO and the other stations. To compensate for this, we plot the recovered signal versus group speed rather than time thus accounting for the different path length. Relocating the earthquake by roughly 6 km to the south-east relative to the PDE location improved the match between the earthquake and cross-correlation signals. Examples such as this give confidence to the ability to interpret cross-correlations of ambient noise in terms of earth structure, similar to the way earthquake signals are interpreted. Coincidences between earthquake and station locations are, however, too rare to be of general use for data selection or uncertainty estimation.

The principal metric on which to base a judgment of the quality of the measurements is stability, the robustness of the measurement to perturbations in the conditions under which it is obtained. The stability of spatially clustered and temporally repeated measurements is particularly useful to identify erroneous measurements and to quantify uncertainties.

Clustering measurements obtained at a particular station from a set of earthquakes located near to one another is commonly used to assess uncertainties in earthquake dispersion measurements (e.g., Ritzwoller and Levshin, 1998). A similar cluster analysis can be applied to ambient noise data. For example, Figure 16 presents a spatial cluster analysis that exploits the high station density in southern California. Numerous measurements between southern California and distant stations were obtained with similar paths (see Fig. 16a). Cross-correlations between the southern California stations and the GSN station ANMO provide one estimate of uncertainty. In this example that there is substantial difference in velocity compared to the CU-Boulder global model (Shapiro and Ritzwoller, 2002) at periods below about 35 sec for group speeds and 30 sec for phase speeds. Measurements between southern California and more distant stations typically are closer to the model prediction. Spatial cluster analyses such as this when a tight cluster of stations subtends a small angle to a relatively distant station (located many inter-station spacings away from the cluster). These conditions typically will not hold for most measurements, although the growth of regional arrays like the Transportable Array component of USArray/EarthScope will help to make this method increasingly applicable. At present, however, cluster analysis provides only an assessment of average uncertainty for long path measurements or a data rejection criterion for

a subset of the measurements.

A more useful method to estimate reliability is to assess temporal repeatability. The physical basis for this method is that sources of ambient noise change seasonally and provide different conditions for the measurements. Given the changing conditions, therefore, the repeatability of a measurement is a significant indicator of reliability. This standard is elevated to a high position in our assessment, as we equate seasonal repeatability with measurement uncertainty. It is one of the salutary features of ambient noise dispersion measurements generally that uncertainties can be measured in this way, unlike earthquake derived measurements.

Figure 17 presents an example of seasonal variability for the GSN station-pair CCM and DWPF. Four disjoint 3-month broad-band cross-correlations are shown in Figure 17a comprising winter, spring, summer, and fall months. The long period part of the cross-correlations displays a strong seasonal variability. Group velocity curves from individual 3-month stacks are plotted in Figure 17b. Using a year of data, in principle there are twelve 3-month stacks; i.e., Jan-Feb-Mar, Feb-Mar-Apr, ..., Dec-Jan-Feb. Only curves from the 3-month stacks in which spectral SNR > 10 at all periods are shown. Ten of the twelve stacks satisfied this criterion. Overplotted with the red line is the group speed curve measured for the 12-month stack. It appears in the middle of the shorter measurements and is smoother than most of the 3-month stacks. This indicates that the use of variability among the 3-month stacks to estimate the uncertainty in the dispersion measurement for the 12-month time-series is conservative. The predicted curve from the 3-D model of Shapiro and Ritzwoller (2002) is also overplotted in green.

In earlier applications of the data processing procedure described herein (Yang et al., 2007; Lin et al., 2007a), dispersion measurements are obtained on 12-months of data. To estimate uncertainties in these measurements, we also measure dispersion on all sequential 3-month stacks if signal-to-noise (SNR) exceeds some threshold. The standard-deviation is computed if a sufficient number of the 3-month stacks exceeds the SNR criterion. In the high ambient noise environment of New Zealand, Lin et al. (2007a) required seven of the 3-month stacks to have SNR > 10. Yang et al. (2007), working with the lower ambient noise conditions

that prevail across most of Europe yielded lower SNR values of the resulting cross-correlations. They were forced to loosen this criterion (four 3-month stacks with SNR > 7). Both studies rejected any measurement for which an uncertainty measurement could not be determined. Yang et al. (2007), in particular, rejected many measurements because uncertainty could not be determined even with the loosened criteria. They argued, therefore, that at least across much of Europe, two years of data would be preferable to one in order to estimate uncertainties and reject far fewer measurements. Presumably this would be true for most other continents around the world.

If a seismic station is operated or a pair of stations are run simultaneously only for a short period of time, however, acquisition of two years of data may be out of the question and temporal subsetting to estimate uncertainties may not be feasible. Temporal overlap between neighboring deployments of stations also may not be long enough to estimate uncertainties based on temporal variability. In this case, SNR measurements can provide a useful proxy for uncertainties. An example is shown in Figure 18. In these figures, the average standard deviation measured from the temporal variability of cross-correlations of ambient noise observed over one-year is plotted as a function of spectral SNR. The cross-correlations are obtained on more than 200 stations across the US and southern Canada from the year 2004. Results at 10 sec period (green circles) and 20 sec period (red triangles) are shown, and are segregated into two inter-station distance ranges, 1000 - 2000 km and distances greater than 2000 km. At both periods there is a clear linear relation between standard deviation and spectral SNR for $10 < \text{SNR} < 40$. For $\text{SNR} < 10$, the standard deviation increases rapidly and non-linearly. These curves illustrate that SNR may provide a useful proxy for measurement error if $\text{SNR} > 10$. In addition, because, as Figure 12 shows, SNR is also related to the number of weeks in the stack, the number of weeks stacked is related to the expected measurement uncertainty. For example, inspection of Figure 12 shows that at 10 sec period, a SNR of 10 is expected after 4-weeks of observation. Figure 18a reveals that a SNR of 10 relates to a measurement error of about 55 m/sec. Thus, four-weeks of observation (in North America) is expected to give a measurement error of about 55 m/sec. Increasing the observing length to 20 weeks at 10 sec period is expected to increase the SNR to about 20 and the measurement

error is expected to reduce to about 45 m/sec. Observing still longer to 60 weeks is expected, on average, to increase SNR to about 30 and reduce error to about 35 m/sec. Thus, although it is tempting to stack data indefinitely, the power-law dependence of SNR on time-series length generates diminishing returns in reducing measurement errors after SNR is high enough to provide a reasonable dispersion measurement. Continued observation past this point may best be used to measure temporal variability directly, which is preferable over the use of proxy curves.

The discussion in the previous paragraph is relevant to the design of seismic experiments to use ambient noise cross-correlation. It is, however, intended to be more illustrative than definitive, and more work is needed to understand the distributions of the quantities in order to produce better proxy curves and guide their use.

Third, we seek measurements that cohere as a whole; that is, that agree with other accepted measurements. This condition can be tested tomographically. Measurements that can be fit with a smooth tomographic map are said to agree with one another. Yang et al. (2007) presents a detailed discussion of the application of this criterion across Europe. He finds that, on average, dispersion measurements that derive from ambient noise tomography can be fit better than those that derive from earthquake data. Moreover, the distribution of misfit is tight. While erroneous measurements do pass the previous selection criteria, they are small in number. An example comparison between the misfit histograms of ambient noise and earthquake derived group speed measurements across Europe is shown in Figure 19.

6. Summary and conclusions

The data processing procedure for extracting estimated Rayleigh wave Green functions from ambient seismic noise has now largely stabilized and is sufficiently well evolved to describe without fear of radical modification in the near future. The procedures that are described herein have been designed not only to deliver reliable measurements, but to be flexible and applicable to a wide variety of observational settings. The procedure divides into four phases: (1) single-station data preparation, (2) cross-correlation and stacking to a desired time-series length, (3) dispersion measurement, and (4) quality control. Because the number

of cross-correlations grows as the square of the number of stations, the procedure we describe is entirely automated.

The principal step in single-station data preparation is "temporal normalization" which is designed to ameliorate the contamination of the ambient noise signals by earthquakes, instrument irregularities, and non-stationary noise sources near to stations (such as passing storms and high local sea heights). We advocate the use of "running-absolute-mean" normalization, which is an effective method that allows for tuning to regional earthquake conditions. In addition, spectral whitening is advisable prior to cross-correlation in order to minimize contamination by the 26 sec Gulf of Guinea resonance and to broaden the measurement band.

The use of long time-series helps to optimize signal-to-noise ratio (SNR), which is anti-correlated with measurement error. SNR displays a power law dependence on time-series length, with the most rapid emergence of signals from noise in the microseismic (< 20 sec period) and "Earth hum" (> 50 sec) bands. The greatest challenge for ambient noise tomography, therefore, lies between about 30 sec and 60 sec period.

Automated dispersion measurement is performed with a modification of traditional frequency-time analysis (e.g., Levshin et al., 1992). We have described methods that measure group velocity curves reliably with and without phase-matched filtering. Phase-matched filters are helpful to extract the estimated Green function from adjacent contaminating signals, if they exist. However, phase-matching filtering works best on broad-band waveforms. For signals that are significantly band-limited, it would be best to forego phase-matched filtering. Reliable group velocity measurements, on average, require a SNR > 10.

Experience reveals that reliable group velocity measurements require an inter-station spacing, Δ in km, of at least three wavelengths. This creates a period cut-off $\tau_{\max} \sim \Delta/12$. At periods longer than this, the inter-station spacing will be less than three wavelengths, and the measurements are significantly more likely to be unreliable. This condition can impose a stringent constraint on the use of ambient noise tomography with data from local or regional arrays.

Phase velocity curves also emerge naturally from the automated frequency-time analysis

and preliminary results indicate that the curves are stable and smooth as long as SNR is above a threshold value of about 10. For small inter-station spacings where only short period phase velocities can be measured, the 2π phase-ambiguity may be difficult to resolve unless station density is high enough to exploit the observed phase "move-out". Further work is also needed to determine if the period cut-off can be relaxed for phase velocity measurements.

Within the context of an automated data processing procedure, data quality control measures are particularly important to identify and reject bad measurements and compute quality assurance statistics for the accepted measurements. The principal metric on which to base a judgment of quality is stability, the robustness of the measurement to perturbations in the conditions under which it is obtained. Temporal repeatability, in particular, is a significant indicator of reliability. The physical basis for this method is that sources of ambient noise change seasonally and provide different conditions for the measurements. This standard is elevated to a high position in our assessment, as we equate seasonal repeatability with measurement uncertainty. It is one of the commendable features of ambient noise dispersion measurements generally that uncertainties can be measured, unlike earthquake derived measurements. Although one year of data is sufficient to estimate uncertainties through temporal repeatability in some cases, two years of data are preferable.

Acquisition of one to two years of data may be out of the question in many circumstances, so that temporal subsetting to estimate uncertainties may not be feasible. In this case, SNR measurements can provide a meaningful proxy for uncertainties. Such proxy curves relating measurement uncertainty to SNR (e.g., Figure 18) can be used with information about the emergence rate of the signal (e.g., Figure 10) to help design experiments that seek to perform ambient noise tomography. The results in Figure 18 are are not yet definitive, and more work is needed to understand the statistical distributions of the quantities in order to produce better proxy curves and guide their use. Nevertheless, we believe that this approach promises to provide approximate uncertainty estimates for experiments that are too short to exploit temporal repeatability.

The data processing procedures that have been developed for ambient noise tomography currently have a history shorter than three years and need to continue to develop. In particular,

efforts are needed to tune the method further for phase velocities (e.g., understanding potential phase ambiguities related to source distribution) and Love waves. We also believe that work on proxy curves in which SNR (or time-series length) is used to infer an expected measurement uncertainty is a fertile area for future research.

Acknowledgments

The authors thank Roel Snieder for a discussion of the $\pi/4$ phase term that appears in equation (11). All of the data used in this research were downloaded either from the IRIS Data Management Center, the European Orfeus Data Center, or the New Zealand GeoNet Data Center. This research was supported by a contract from the US Department of Energy, DE-FC52-2005NA26607, and two grants from the US National Science Foundation, EAR-0409217, EAR-0408228, and EAR-0450082.

References

Bensen, G.D., M.H. Ritzwoller, N.M. Shapiro, A.L. Levshin (2005). Extending ambient noise surface wave tomography to continental scales: Application across the United States, *EOS Trans. AGU*, **86**(52), Fall Meeting Suppl., Abstract S31A-0274.

Bracewell, R.N. (1978). *The Fourier Transform and its Applications*, McGraw-Hill, 2nd edition, New York.

Campillo M. and A. Paul (2003). Long-range correlations in the diffuse seismic coda, *Science*, **299**, 547-549.

Cho, K.H., R.B. Hermann, C.J. Ammon, and K. Lee (2006). Imaging the crust of the Korean peninsula by surface wave tomography, *Bull. Seism. Soc. Am.*, submitted.

Crawford, W.C., R.A. Stephen, and S.T. Bolmer (2006). A second look at low-frequency marine vertical seismometer data quality at the OSN-1 stie off of Hawaii for seafloor, buried and borehole emplacements, *Bull. Seism. Soc. Amer.*, **96**, 1952-1960.

Derode, A., E. Larose, M. Tanter, J. de Rosny, A. Tourim, M. Campillo, and M. Fink (2003). Recovering the Green's function from field-field correlations in an open scattering medium, *J. Acoust. Soc. Am.*, **113**, 2973-2976.

Dziewonski, A.M., S. Bloch, and M. Landisman (1969). A technique for the analysis of transient seismic signals, *Bull. Seism. Soc. Am.*, **59**, 427-444.

Ekstrom, G., J. Tromp, and E.W.F. Larson (1997). Measurements and global models of surface wave propagation, *J. Geophys. Res.*, **102**, 8137-8157.

Herrin, E.E. and T.T. Goforth (1977). Phase-matched filters: Application to the study of Rayleigh Waves, *Bull. Seism. Soc. Am.*, **67**, 1259-1275.

Holcomb, L.G. (1998). Spectral structure in the Earth's microseismic background between 20 and 40 seconds, *Bull. Seism. Soc. Am.*, **88**, 744-757.

Larose, E., A. Derode, M. Campillo, and M. Fink (2004). Imaging from one-bit correlations of wideband diffuse wavefields, *J. Appl. Phys.*, **95**, 8393-8399.

Larose, E., A. Derode, D. Corennec, L. Margerin, and M. Campillo (2005). Passive retrieval of Rayleigh waves in disoredered elastic media, *Phys. Rev. E.*, **72**, 046607, doi:10.113/PhysRevE.72.046607.

Levshin, A.L., V.F. Pisarenko, and G.A. Pogrebinsky (1972). On a frequency-time analysis of oscillations, *Ann. Geophys.*, **28**, 211 - 218.

Levshin, A.L., T.B. Yanovskaya, A.V. Lander, B.G. Bukchin, M.P. Barmin, L.I. Ratnikova, and E.N. Its (1989). *Seismic Surface Waves in a Laterally Inhomogeneous Earth*, edited by V.I. Keilis-Borok, Kluwer, Norwell, Mass.

Levshin, A.L., L. Ratnikova, and J. Berger (1992). Peculiarities of surface wave propagation across central Eurasia, *Bull. Seism. Soc. Am.*, **82**, 2464-2493.

Levshin, A.L., M.H. Ritzwoller, and J.S. Resovsky (1999). Source effects on surface wave group travel times and group velocity maps, *Phys. Earth Planet. Int.*, **115**, 293 - 312, 1999.

Levshin, A.L. and M.H. Ritzwoller (2001). Automated detection, extraction, and measurement of regional surface waves, *Pure Appl. Geophys.*, **158**(8), 1531 - 1545.

Lin, F.-C., M.H. Ritzwoller, and N.M. Shapiro (2006). Is ambient noise tomography across ocean basins possible?, *Geophys. Res. Lett.*, **33**, L14304, doi:10.1029/2006GL026610.

Lin, F.-C., M.H. Ritzwoller, J. Townend, M. Savage, and S. Bannister (2007a). Ambient noise Rayleigh wave tomography of New Zealand, *Geophys. J. Int.*, in press.

Lin, F.-C., M.P. Moschetti, and M.H. Ritzwoller (2007b). Surface wave tomography of western United States from ambient noise study: Phase velocity maps for Rayleigh and Love waves, in preparation.

Moschetti, M.P., M.H. Ritzwoller, and N.M. Shapiro (2007). Ambient noise tomography from the first two years of the USArray Transportable Array: Group speeds in the western US, *Geophys. Res. Lett.*, submitted.

Paul, A., M. Campillo, L. Margerin, E. Larose and A. Derode (2005). Empirical synthesis of time-asymmetrical Green function from the correlation of coda waves, *J. Geophys. Res.*, **110**, doi:10.1039/2004JB003521.

Rhie, J., and B. Romanowicz (2004). Excitation of earths incessant free oscillations by Atmosphere-Ocean-Seafloor coupling, *Nature*, **431**, 552-556.

Ritzwoller, M.H., and A.L. Levshin (1998). Surface wave tomography of Eurasia: group velocities, *J. Geophys. Res.*, **103**, 4839-4878.

Roux, P., K.G. Sabra, P. Gerstoft, W.A. Kuperman, and M.C. Fehler (2005). P-waves from cross-correlation of seismic noise, *Geophys. Res. Lett.*, **32**, L19393, doi:10.1029/2005GL023803.

Russell, D.W., R.B. Herrman, and H. Hwang (1988). Application of frequency-variable filters to surface wave amplitude analysis, *Bull. Seism. Soc. Am.*, **78**, 339 - 354.

Sabra, K.G., P. Gerstoft, P. Roux, W.A. Kuperman, and M.C. Fehler (2005a). Extracting time-domain Green's function estimates from ambient seismic noise, *Geophys. Res. Lett.*, **32**, L03310, doi:10.1029/2004GL021862.

Sabra, K.G., P. Gerstoft, P. Roux, W.A. Kuperman, and M.C. Fehler (2005b). Surface wave tomography from microseism in southern California, *Geophys. Res. Lett.*, **32**, L14311, doi:10.1029/2005GL023155.

Shapiro, N.M. and M.H. Ritzwoller (2002). Monte-Carlo inversion for a global shear velocity model of the crust and upper mantle, *Geophys. J. Int.*, **151**, 88-105.

Shapiro, N.M., and M. Campillo (2004). Emergence of broadband Rayleigh waves from correlations of the ambient seismic noise, *Geophys. Res. Lett.*, **31**, L07614, doi:10.1029/2004GL019491.

Shapiro, N.M., M. Campillo, L. Stehly, and M.H. Ritzwoller (2005). High resolution surface wave tomography from ambient seismic noise, *Science*, **307**, 1615-1618.

Shapiro, N.M., M.H. Ritzwoller, and G.D. Bensen, (2006). Source location of the 26 sec microseism from cross correlations of ambient seismic noise, *Geophys. Res. Lett.*, **33**, L18310, doi:10.1029/2006GL027010.

Snieder, R. (2004). Extracting the Green's function from the correlation of coda waves: A derivation based on stationary phase, *Phys. Rev. E*, **69**, 046610.

Trampert, J. and J.H. Woodhouse (1995). Global phase velocity maps of Love and Rayleigh waves between 40 and 150 sec, *Geophys. J. Int.*, **122**, 675-690.

Wapenaar, K. (2004). Retrieving the elastodynamic Green's function of an arbitrary inhomogeneous medium by cross correlation, *Phys. Rev. Lett.*, **93**, 254301, doi:10.1103/PhysRevLett.93.254301.

Weaver, R.L., and O.I. Lobkis (2001a), Ultrasonics without a source: Thermal fluctuation correlation at MHz frequencies, *Phys. Rev. Lett.*, **87**, doi:10.1103/PhysRevLett.87.134301.

Weaver, R.L. and O.I. Lobkis (2001b). On the emergence of the Green's function in the correlations of a diffuse field, *J. Acoust. Soc. Am.*, **110**, 3011-3017.

Weaver, R.L. and O.I. Lobkis (2004). Diffuse fields in open systems and the emergence of the Green's function, *J. Acoust. Soc. Am*, **116**, 2731-2734.

Yang, Y., M.H. Ritzwoller, A.L. Levshin, and N.M. Shapiro, Ambient noise Rayleigh wave tomography across Europe, *Geophys. J. Int.*, **68**, 259, 2007.

Yao, H., R.D. van der Hilst, and M. V. de Hoop (2006). Surface-wave tomography in SE Tibet from ambient seismic noise and two-station analysis: I. - Phase velocity maps, *Geophys. J. Int.*, **166**, 732-744, doi: 10.1111/j.1365-246X.2006.03028.x.

Received _____

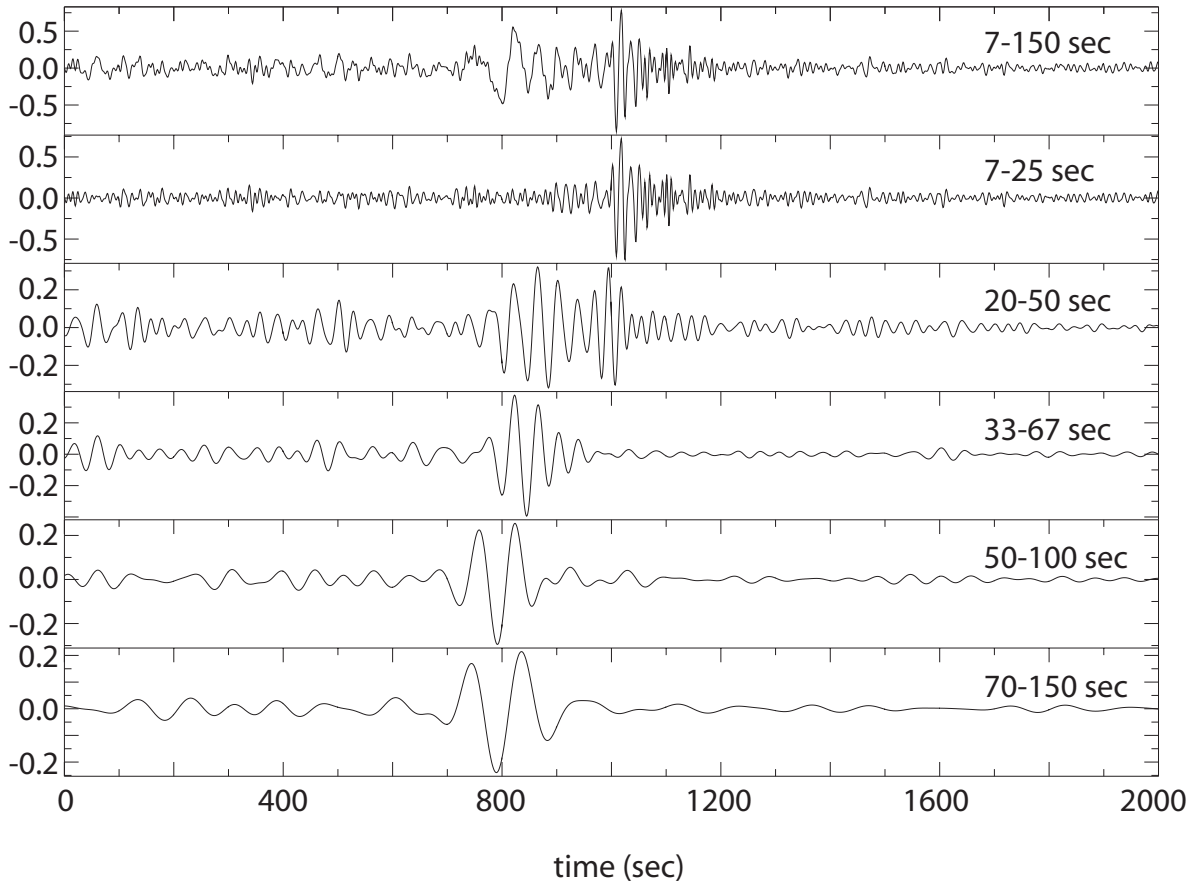

Figure 1. Example of a broad-band symmetric-component cross-correlation using 12-months of data from stations ANMO (Albuquerque, NM, USA) and HRV (Harvard, MA, USA). The broad-band signal (7 - 150 sec pass-band) is shown at top and successively longer period pass-bands are presented lower in the figure. (The symmetric component is the average of the cross-correlation at positive and negative lags.)

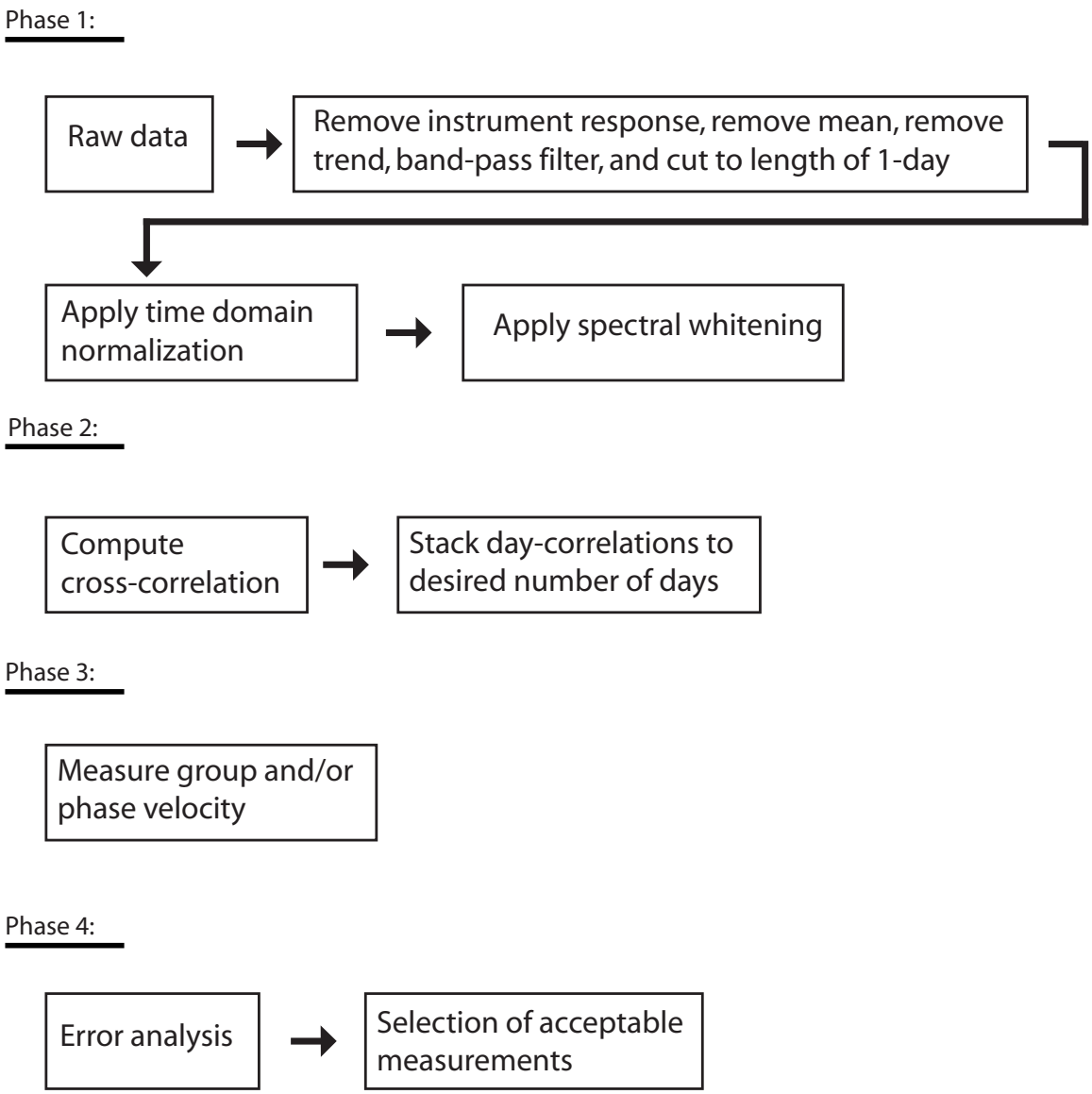

Figure 2. Schematic representation of the data processing scheme. Phase 1 (described in section 2 of the paper) shows the steps involved in preparing single-station data prior to cross-correlation. Phase 2 (section 3) outlines the cross-correlation procedure and stacking, Phase 3 (section 4) includes dispersion measurement and Phase 4 (section 5) is the error analysis and data selection process.

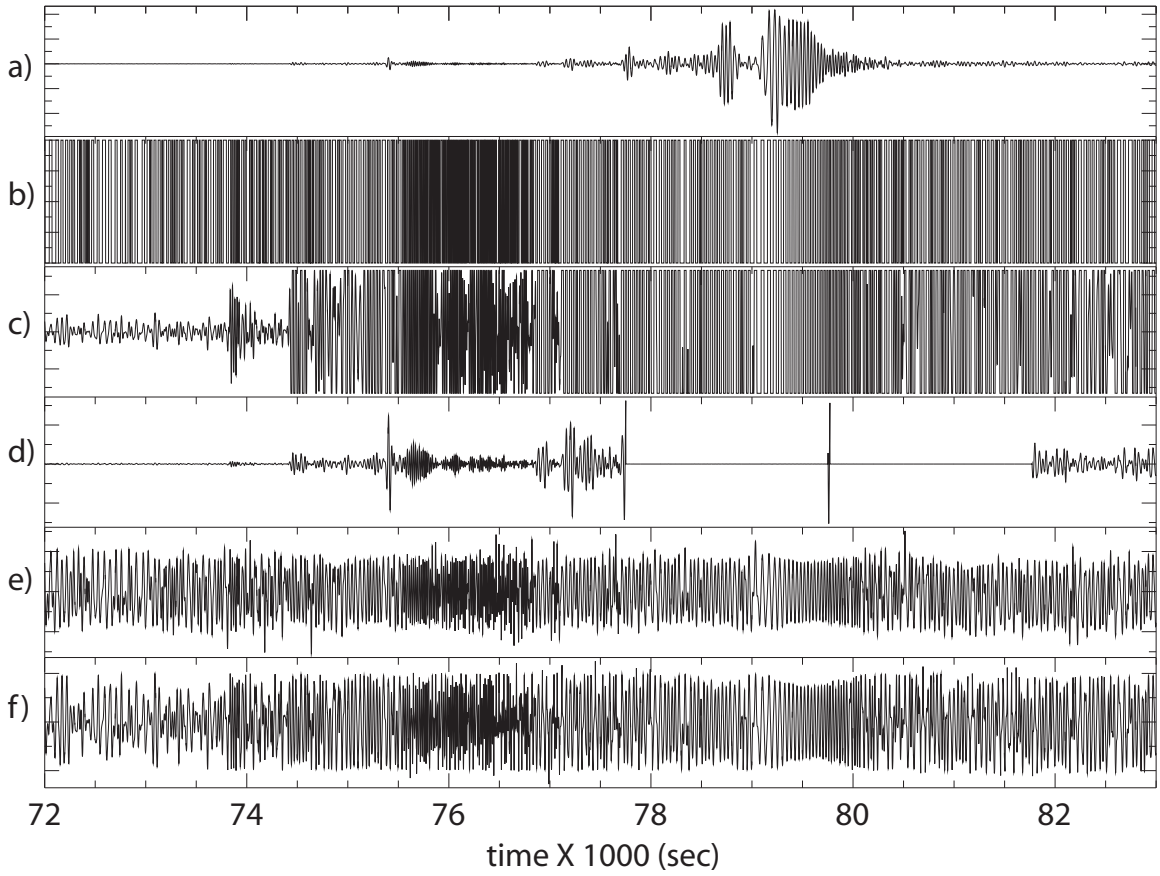

Figure 3. Waveforms displaying examples of the five types of time domain normalization tested. The examples are band-pass filtered between 20 and 100 sec period to clarify the contamination by the earthquake signal. (a) Raw data showing ∼3 hours of data windowed around a large earthquake (Ms = 7.2, Afghanistan-Tajikistan border region) recorded at station ANMO. (b) One-bit normalized waveform, whereby the signal is set to ±1 depending on the sign of the original waveform. (c) Clipped waveform, where the clipping threshold is equal to the root-mean-square (rms) amplitude of the signal for the given day. (d) Automated event detection and removal. If the amplitude of the waveform is above a certain threshold, the next 30 minutes of it are set to zero. (e) Running absolute mean normalization whereby the waveform is normalized by a running average of its absolute value. (f) "Water level normalization" whereby any amplitude above a certain multiple of the daily rms-amplitude is down-weighted. It is run iteratively until the entire waveform is nearly homogeneous in amplitude.

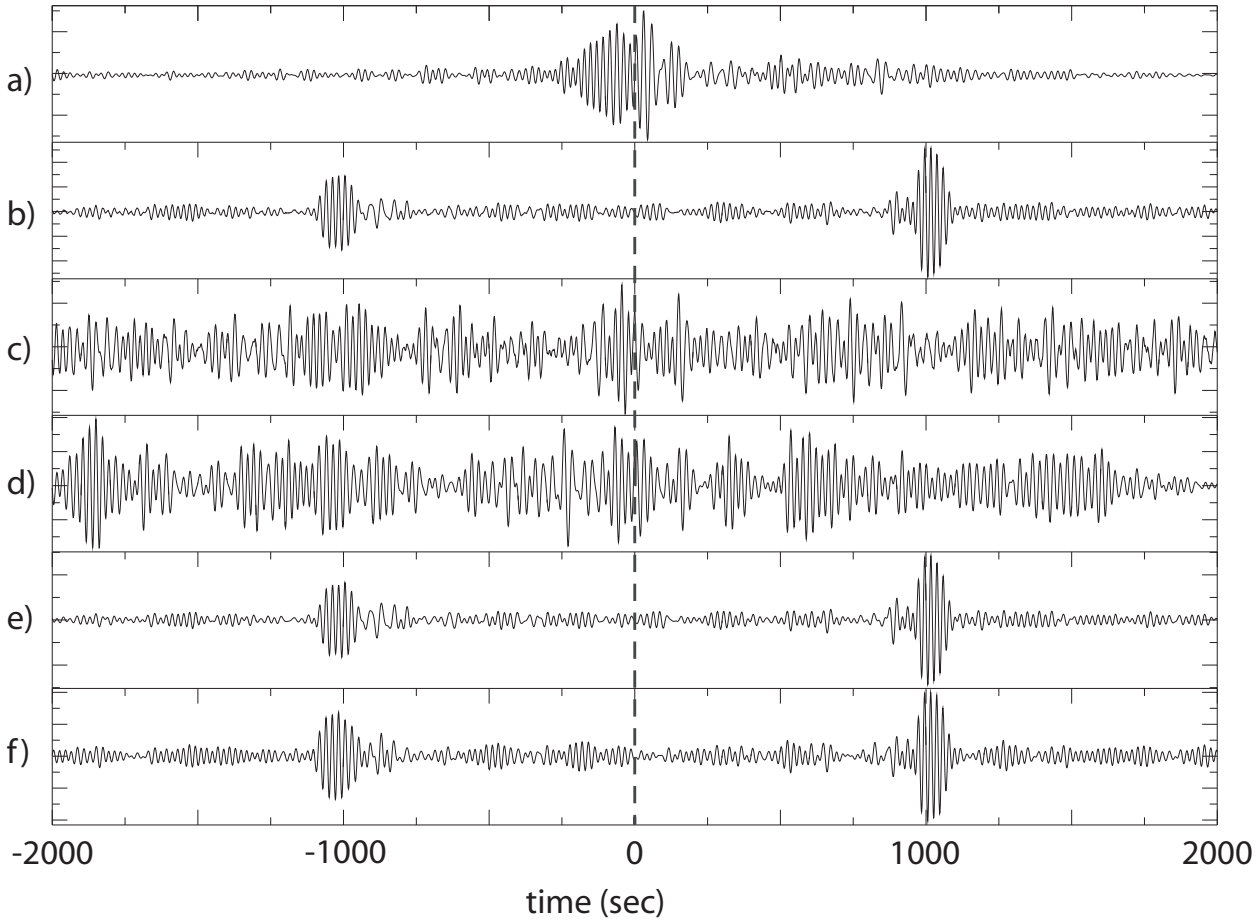

Figure 4. Twelve-month cross-correlations between the station-pair ANMO and HRV for the time-domain normalization methods shown in Figure 3. The pass-band is 20 - 100 seconds period. The panels of the figure (a-f) correspond to those in Figure 3.

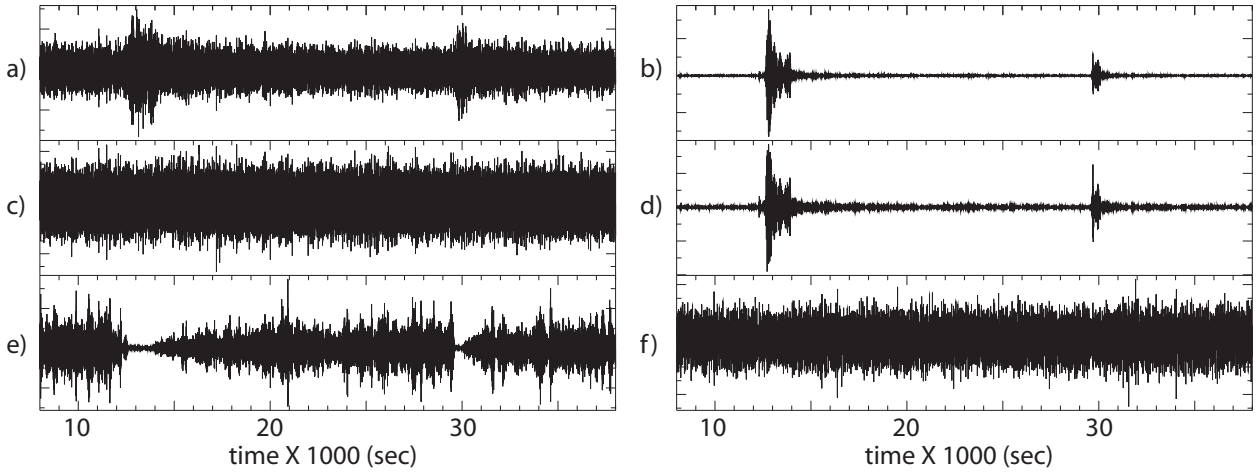

Figure 5. Example of the effect of tuning time-domain normalization to earthquake signals for data from GeoNet station CRLZ in New Zealand. (a) Raw broad-band data from Oct. 14, 2005 showing two earthquakes barely emerging above background noise. (b) Data from (a) band-pass filtered between 15 - 50 sec period, more clearly showing the two earthquake signals (first: S. Fiji, $m_b = 5.4$; second: S. of Kermadec, $m_b = 5.1$). (c) Data after temporal normalization using the running-absolute-mean method in which the weights are defined on the raw (unfiltered) data in (a). (d) Data from (c) band-pass filtered between 15 - 50 sec period, showing that the earthquake signals have not been removed by temporal normalization defined on the raw data. (e) Data after temporal normalization using the running-absolute-mean method in which the weights are defined on the band-pass filtered data in (b). (f) Data from (e) band-pass filtered between 15 - 50 sec period, showing that the earthquake signals have been removed by temporal normalization defined on the band-pass filtered data.

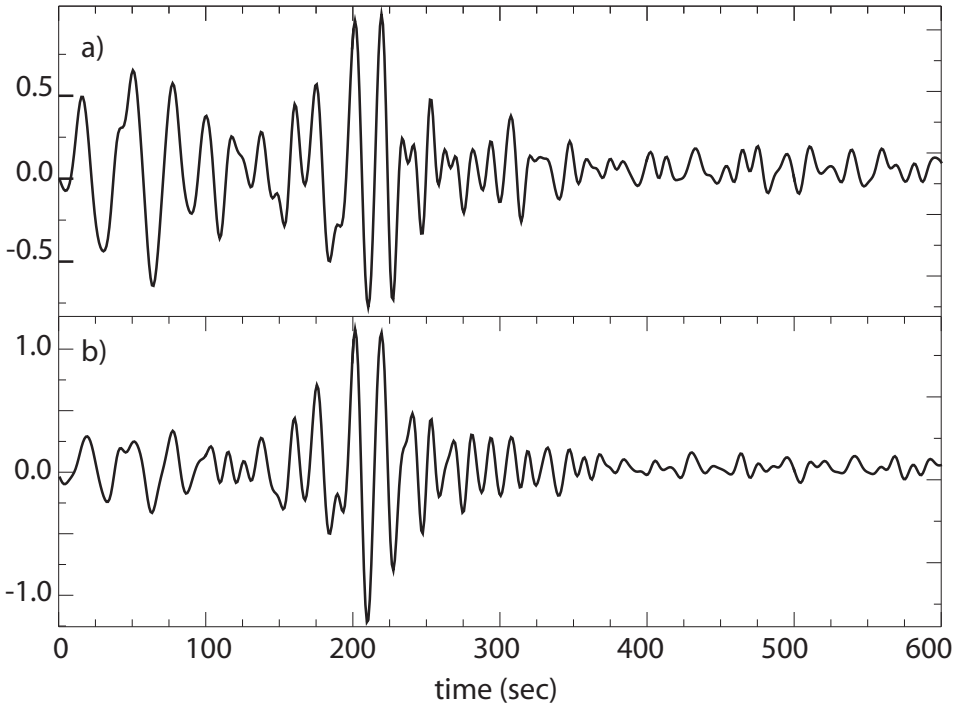

Figure 6. Example of the effect of tuning time-domain normalization to earthquake signals on cross-correlations computed between GeoNet stations CRLZ and HIZ in New Zealand. (a) Year-long cross-correlation in which the temporal normalization is defined on the raw data. (b) Year-long cross-correlation in which the temporal normalization is defined on data band-pass filtered between 15 and 50 sec period. Spurious precursory arrivals are substantially reduced in (b) relative to (a). Waveforms are band-pass filtered between 5 and 50 sec period.

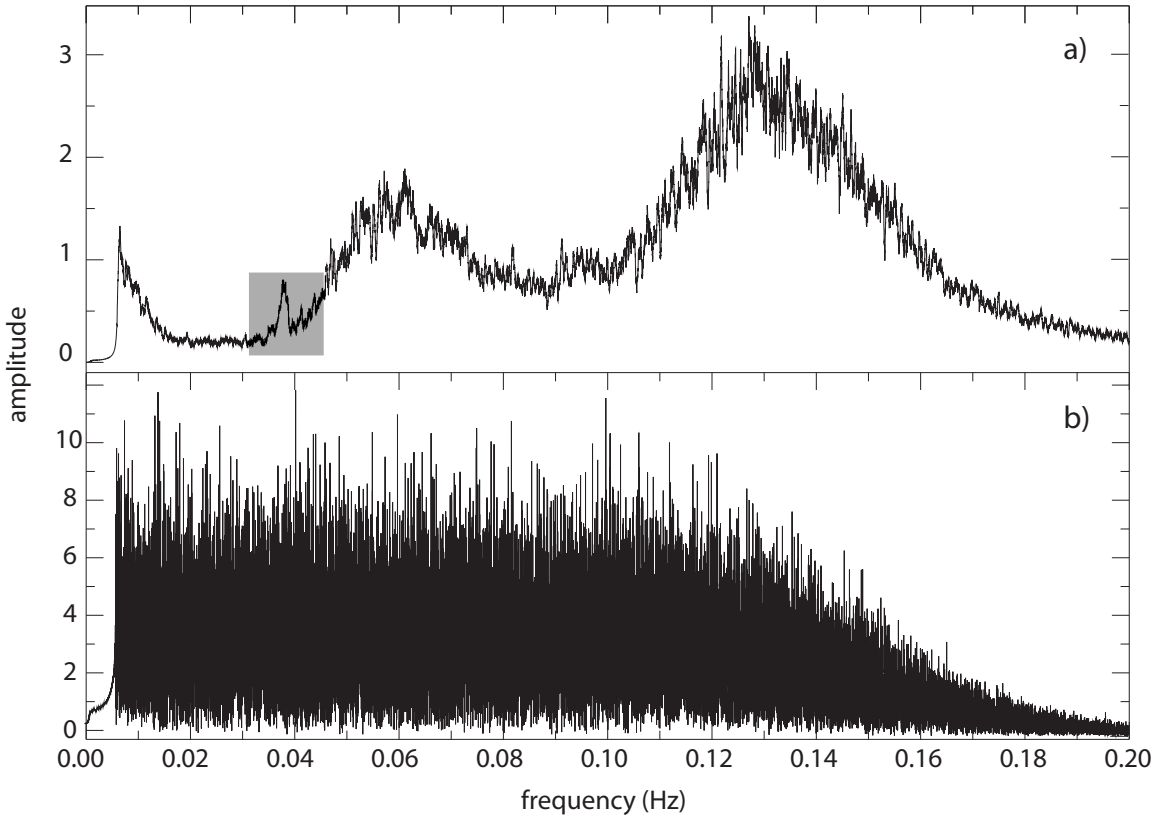

Figure 7. (a) Raw and (b) spectrally whitened amplitude spectra for 1 sample per second vertical component data at station HRV for July 5, 2004. The shaded box indicates the location of the 26 second period signal originating from the Gulf of Guinea. The taper seen at both ends of the spectra is largely attributable to a 7 - 150 second band-pass filter.

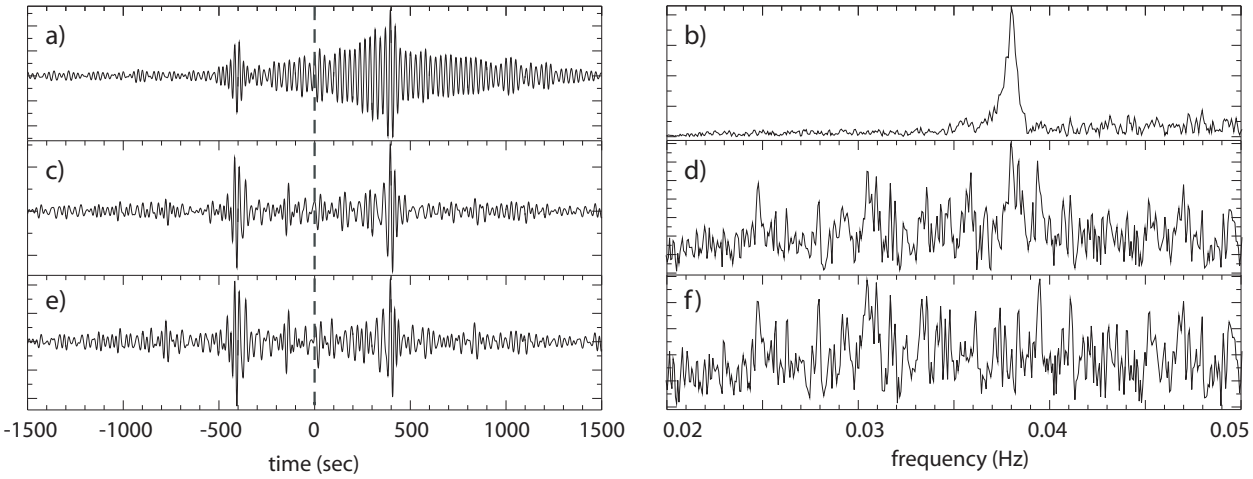

Figure 8. Effect of the 26 sec microseism on cross-correlations and attempts to remove it. (a) Twelve-month cross-correlation between data from stations ANMO and CCM (Cathedral Cave, MO, USA). The broad, nearly monochromatic 26 signal at positive lag dominates the waveform. (b) Amplitude spectrum of the cross-correlation in (a) showing the spectral peak at about 26 sec period. (c) Cross-correlation between data from the same two stations that have been spectrally whitened prior to cross-correlation. (d) Amplitude spectrum of the cross-correlation in (c) showing that the 26 sec spectral peak is largely missing. (e) Cross-correlation between the data that have been spectrally whitened prior to cross-correlation with a notch filter applied around 26 sec period. (f) Amplitude spectrum of the cross-correlation in (e). Application of the notch filter changes the cross-correlation only minimally.

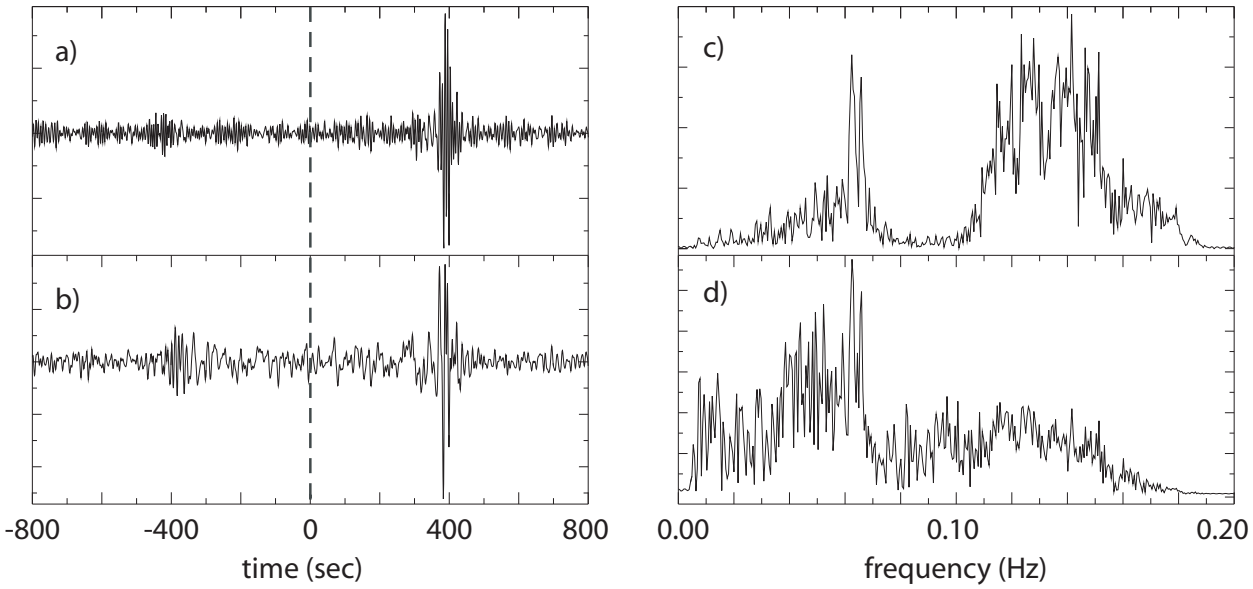

Figure 9. Comparison of cross-correlations with and without spectral whitening. Cross-correlation are for the month April, 2004 for data from stations CCM and SSPA (Standing Stone, PA, USA) band-pass filtered from 7 to 150 seconds period. (a) Cross-correlation without spectral whitening. (b) Cross-correlation with spectral whitening. (c) Amplitude spectrum of the unwhitened waveform in (a). The primary and secondary microseisms dominate the spectrum. (d) Amplitude spectrum of the prewhitened waveform in (b).

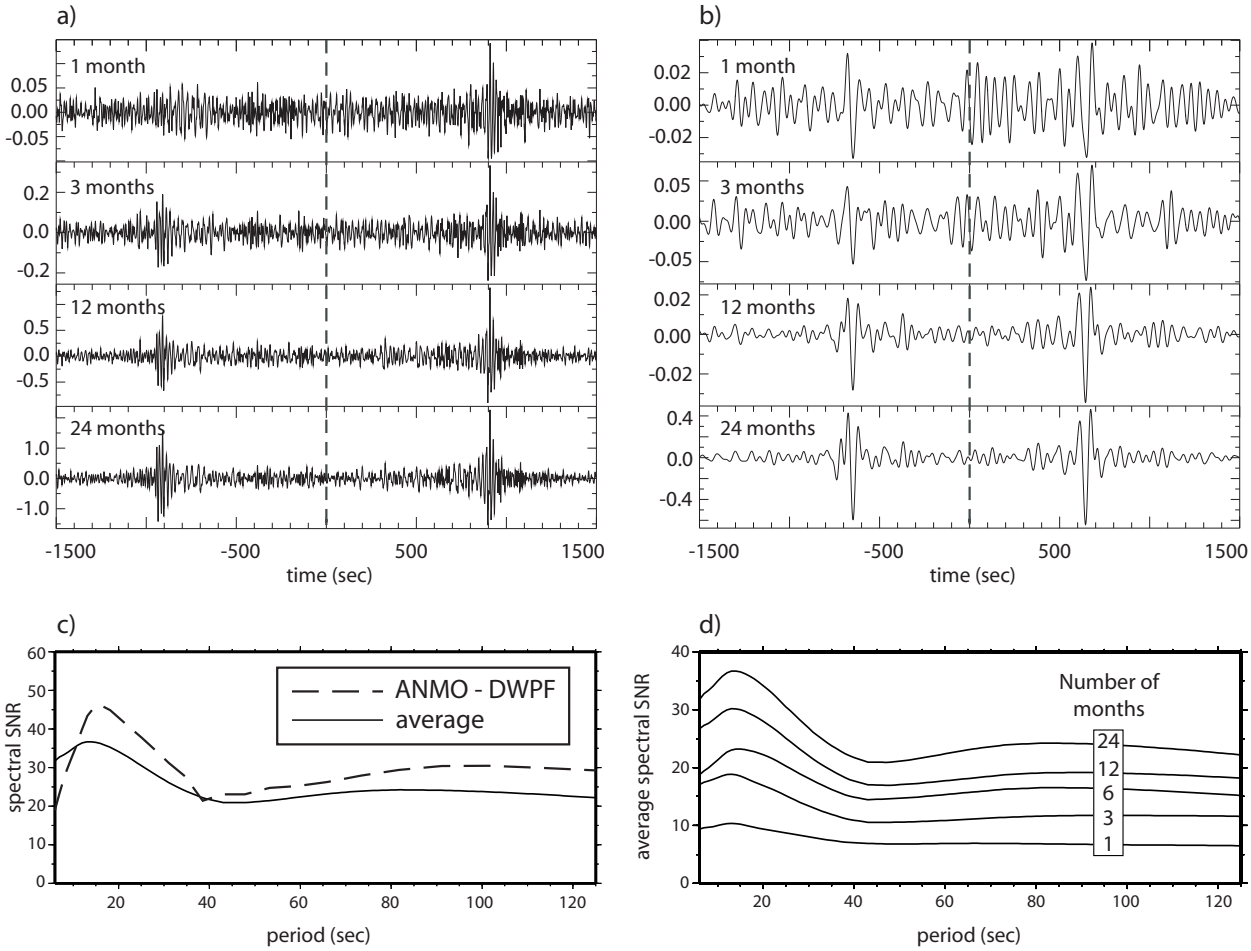

Figure 10. Example of the emergence of the Rayleigh waves for increasingly long time-series. (a) Cross-correlations at the specified time-series lengths for the station pair ANMO and DWPF (Disney Wilderness Preserve, FL, USA) band-passed between 5 to 40 sec period. (b) Same as (a), but for a pass-band between 40 sec to 100 sec period. (c) Spectral SNR for the 24-month ANMO-DWPF cross-correlation shown with a dashed line, and the spectral SNR averaged over all cross-correlations between GSN stations in the US shown with a solid line. (d) Spectral SNR averaged over all cross-correlations between GSN stations in the US for different time-series lengths of 1, 3, 6, 12, and 24 months.

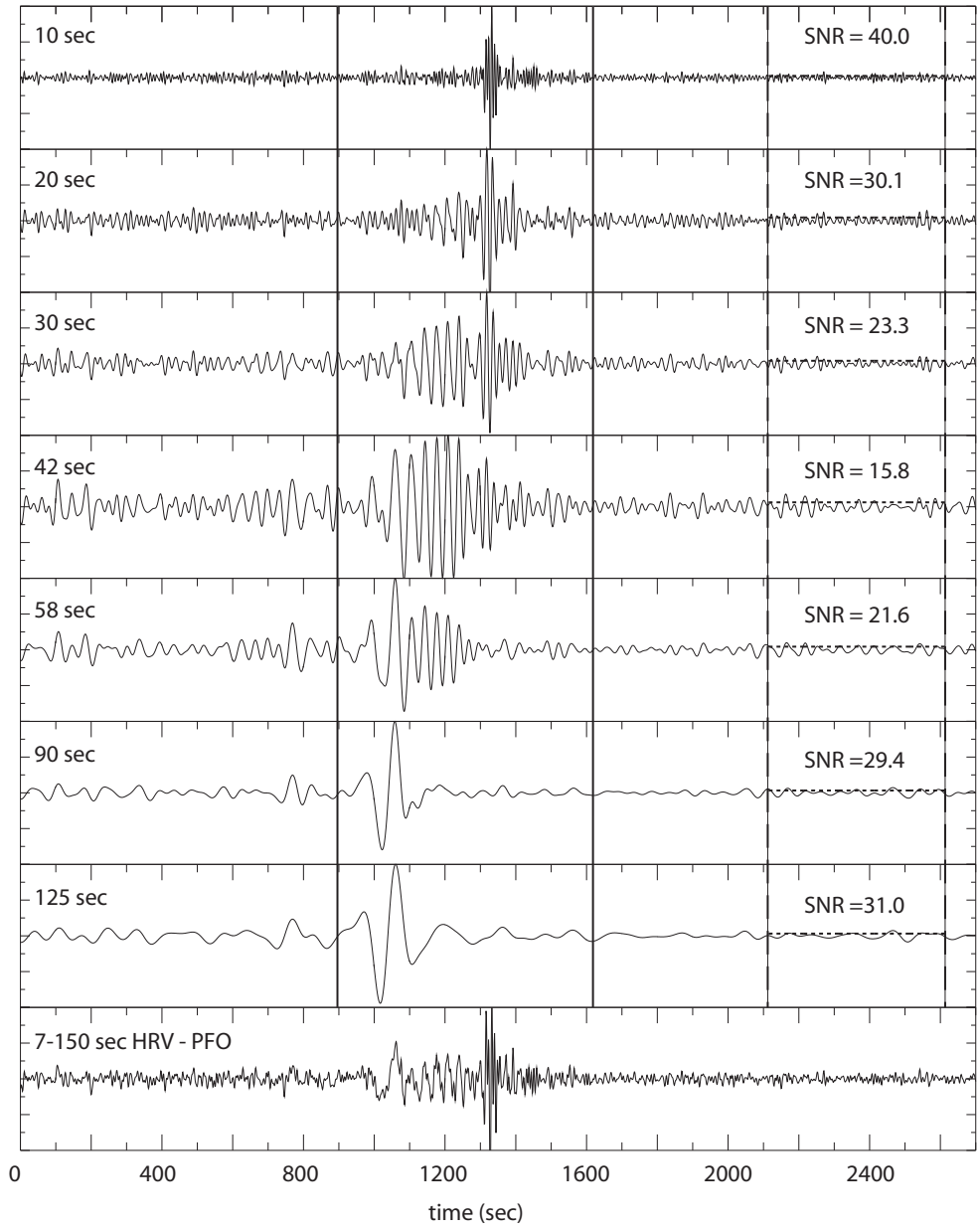

Figure 11. Example of how spectral SNR measurements are obtained on a 12-month cross-correlation between data from stations HRV and PFO (Pinyon Flat, CA, USA). Vertical solid lines indicate the signal windows and vertical dashed lines the noise windows. Waveforms are centered on the period indicated at left in each panel, and SNR is defined as the ratio of the peak within the signal window and rms-noise in the noise window. The noise level is presented as the horizontal dotted lines in the noise windows. SNR in each band is indicated at right in each panel.

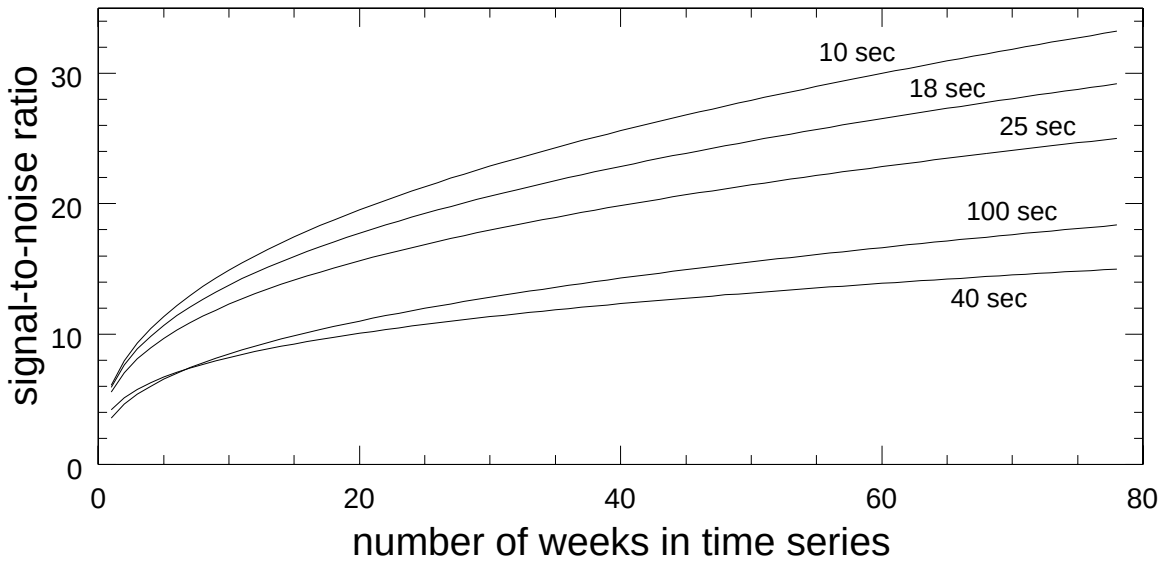

Figure 12. Emergence of the signal with time-series length. The power law fit to the average of the measured SNR from cross-correlations between the GSN stations within the US at each of the five indicated periods is plotted versus variable time-series length (in weeks).

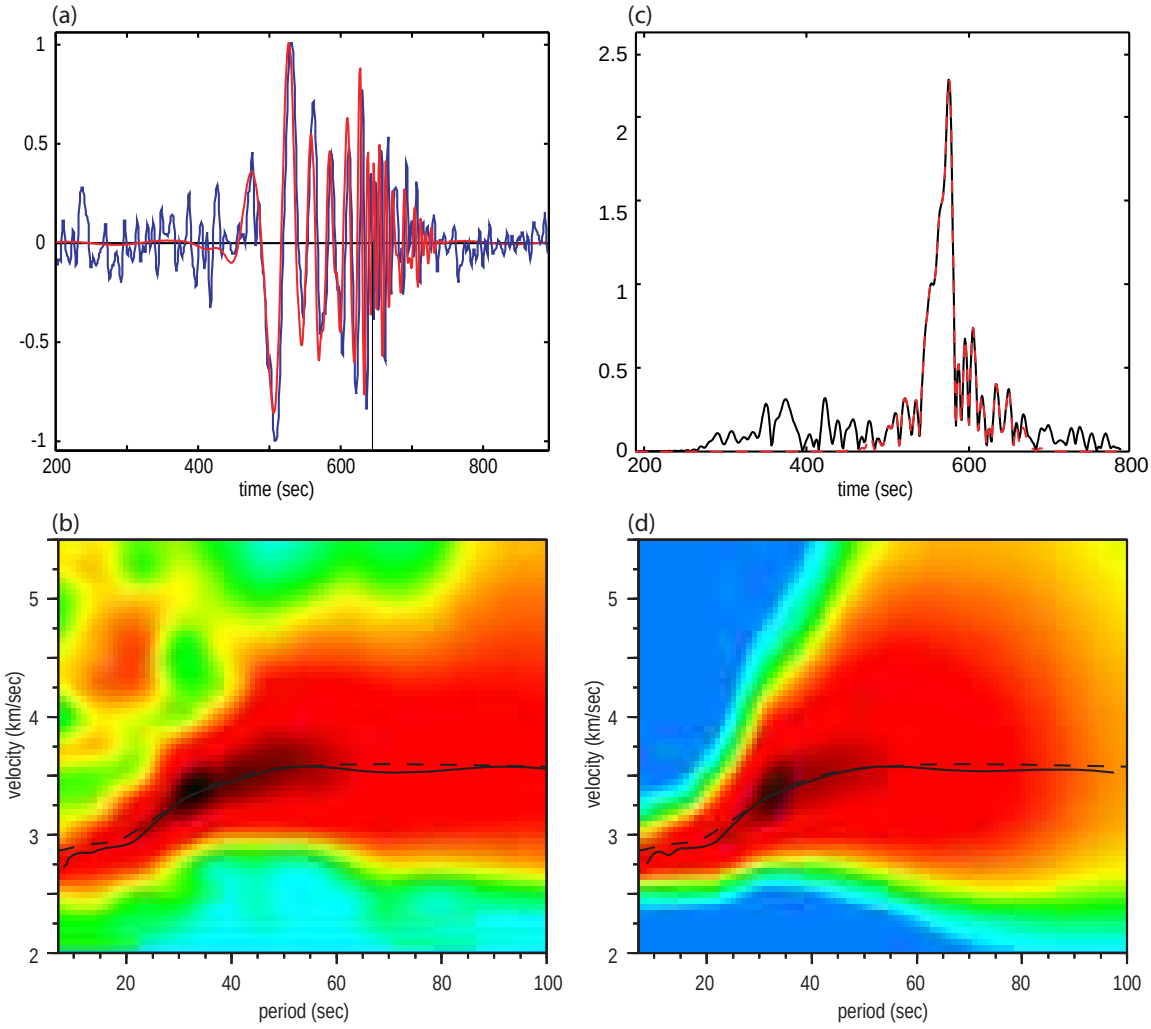

Figure 13. Graphical representation of FTAN. (a) Raw (blue) and cleaned (red) waveforms for the 12-month stacked cross-correlation between stations ANMO and COR (Corvallis, OR, USA). (b) Raw FTAN diagram, measured group speed curve as the solid line, and prediction from the 3-D model of Shapiro and Ritzwoller (2002) as the dashed line. (c) Undispersed or collapsed signal (black) and cleaned signal (red dashed). (d) Cleaned FTAN diagram, measured group speed curve, and prediction from the 3-D model of Shapiro and Ritzwoller (2002).

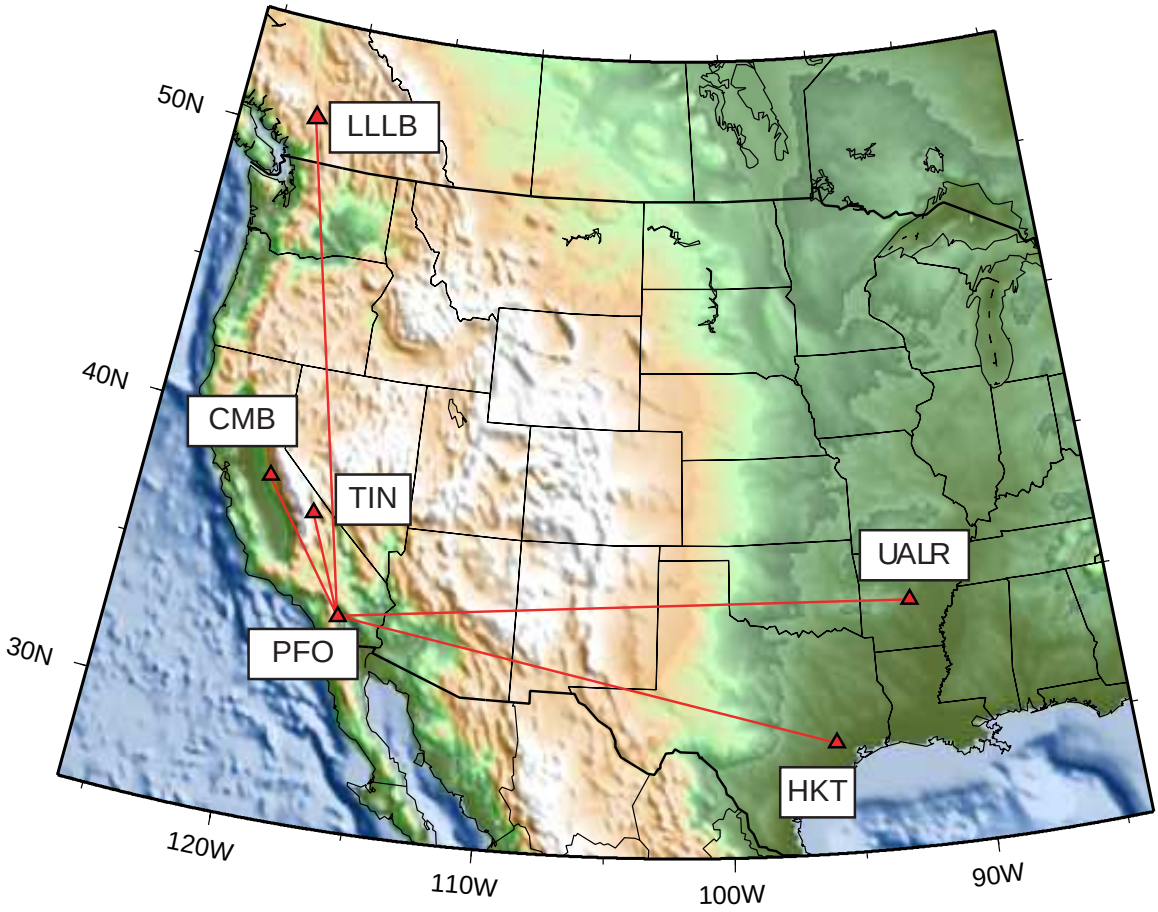

Figure 14. Location map for Figure 15 showing the ray paths between station PFO and the five other stations.

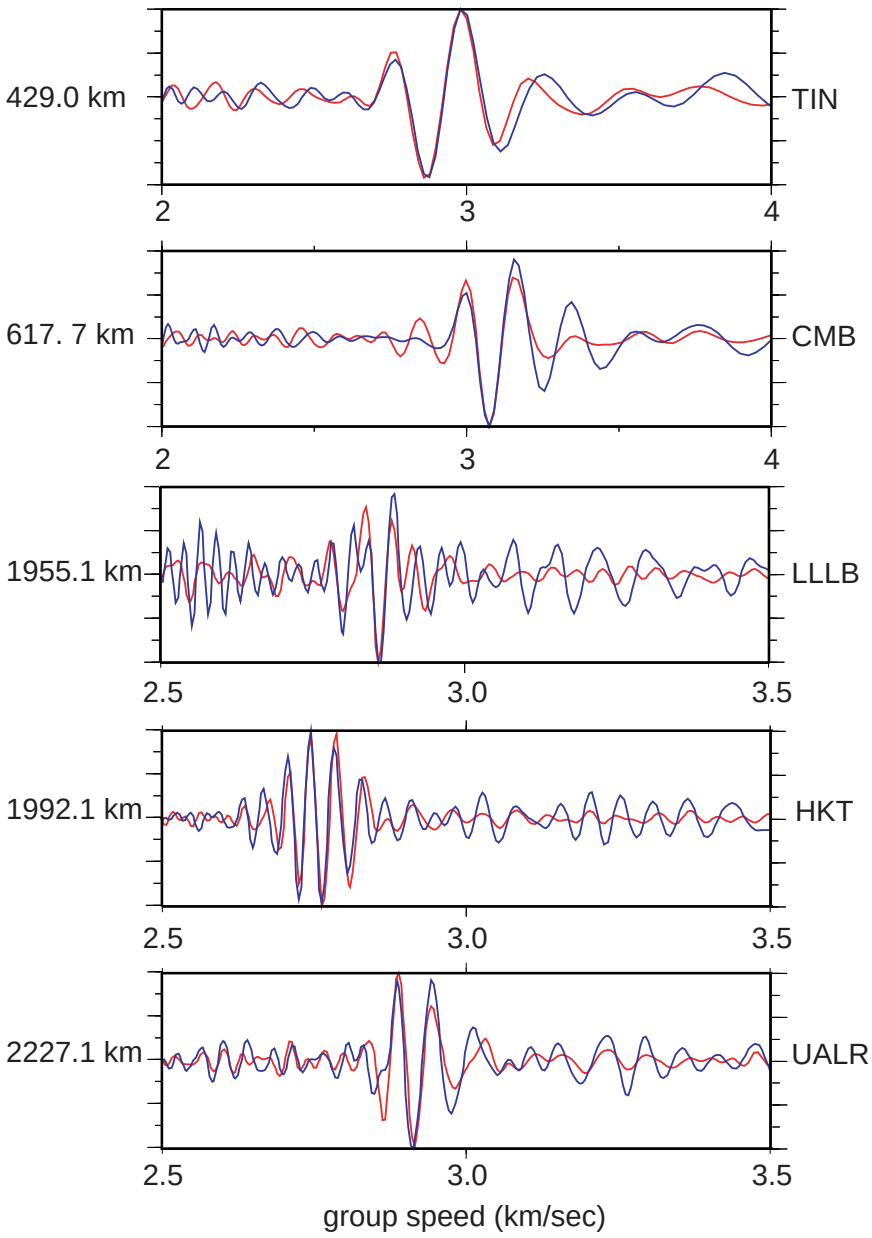

Figure 15. Comparison of symmetric component cross-correlations and earthquake records. Blue lines are 12-month cross-correlations between station PFO in southern California with five other stations around North America. Red lines are earthquake waveforms recorded at the indicated stations following an earthquake near station PFO. The timeseries are plotted against group velocity to account for slightly differing path lengths. Station names are indicated at right and interstation distances are at left. Earthquake records for stations CMB and LLLB are sign flipped.

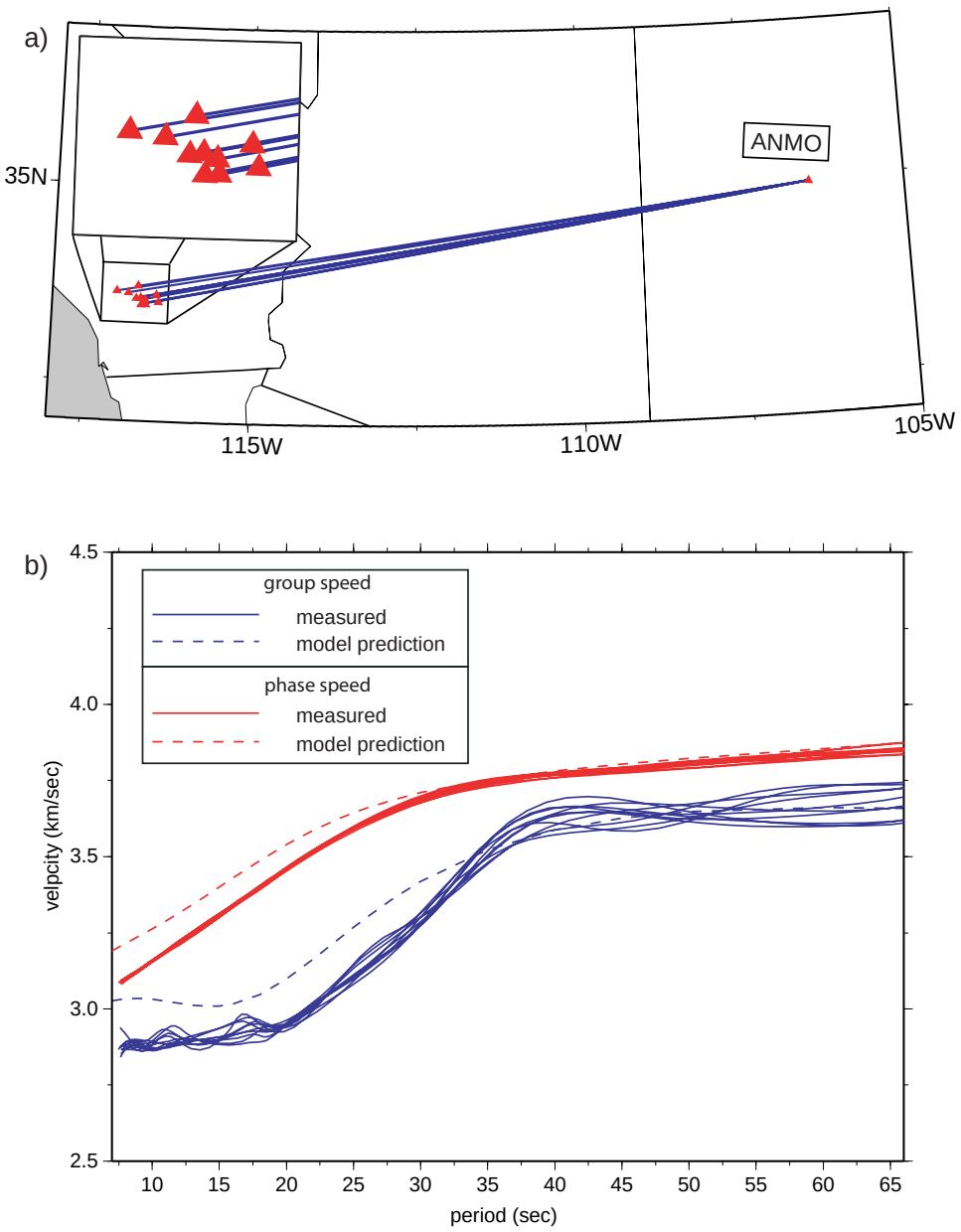

Figure 16. Example assessment of the spatial variability of dispersion measurements using a cluster of 10 stations in southern California. (a) The cluster of 10 paths used in this analysis with a detail plot of the stations used in southern California. (b) Measurements shown with solid lines are from 12-month stacks observed between station ANMO and the southern California cluster of 10 stations and the dashed lines are the predictions from the 3-D model of Shapiro and Ritzwoller (2002).

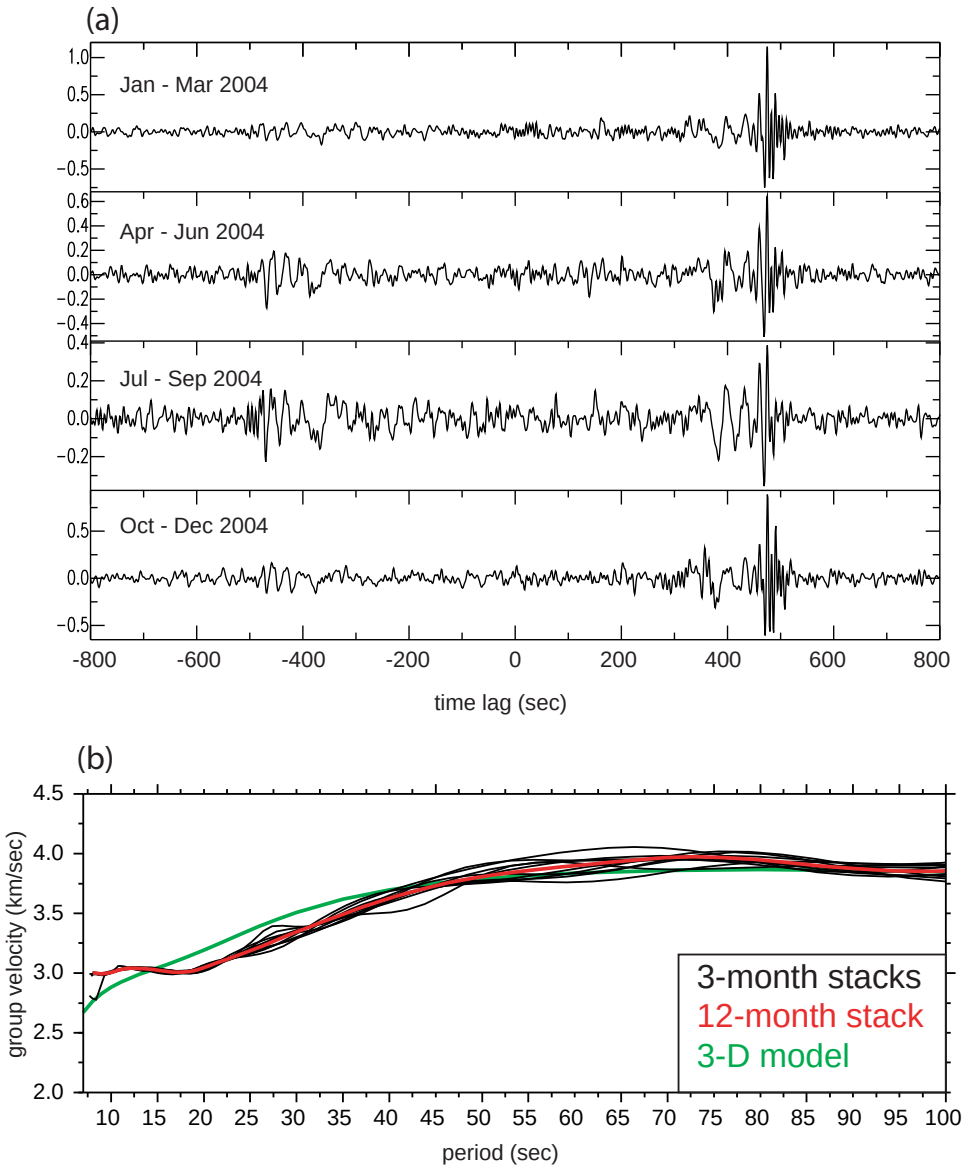

Figure 17. Example assessment of temporal variability of dispersion measurements. (a) Four disjoint broad-band (5 - 150 sec) three-month stacks are shown for the station-pair CCM-DWPF. Arrivals at positive correlation lag are for waves traveling from the northwest, from CCM to DWPF, and negative correlation lag corresponds to waves arriving from the southeast, from DWPF to CCM. (b) Group speed measurements obtained on the symmetric-component from ten 3-months are presented versus period as the black curves. The measurement for the 12-month stack is indicated by the red line and the green line is the prediction from the 3-D model of Shapiro and Ritzwoller (2002).

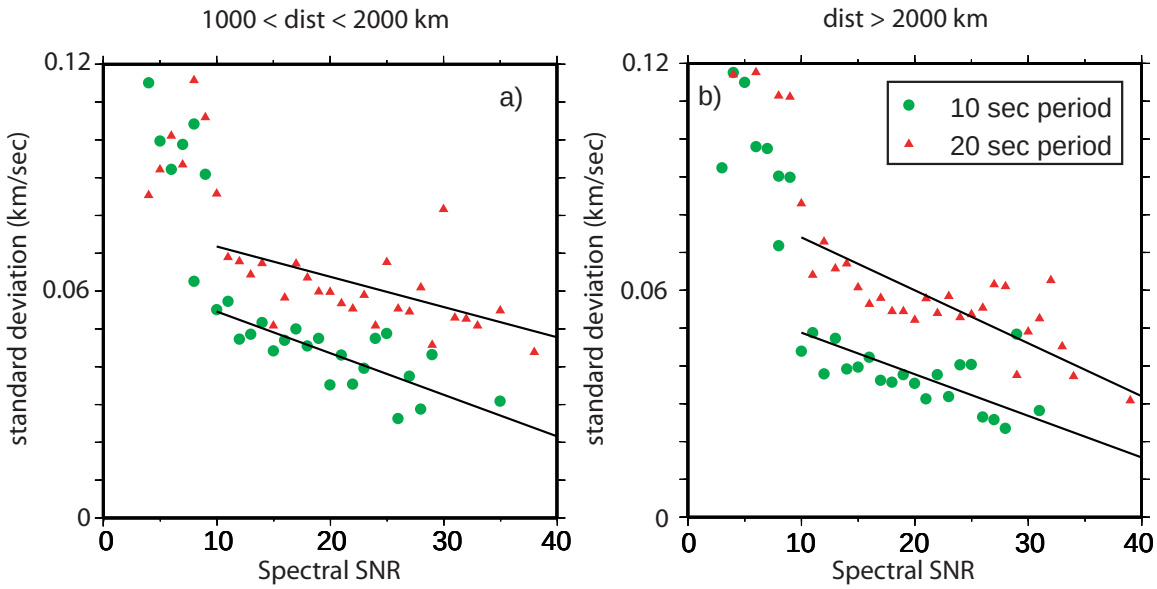

Figure 18. SNR as proxy for measurement uncertainty. Average measurement error, estimated from seasonal variability for a year of data using more than 200 stations across North America, is plotted versus spectral SNR. Two distance ranges are shown and two periods (red triangles - 20 sec; green circles - 10 sec). Below SNR $\sim$ 10, measurements become unreliable. Black lines show the best-fit linear trends for $10 <$ SNR < 40.

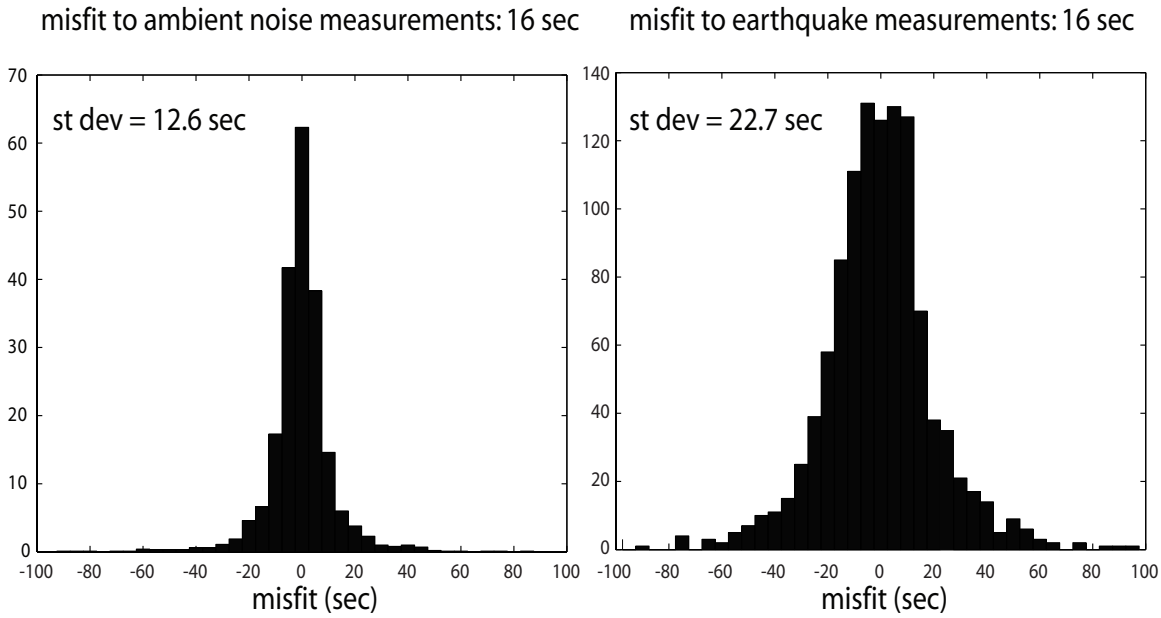

Figure 19. Measurement coherence. Histograms of misfit for ambient noise group time measurements (left) and earthquake group time measurements (right) at 16 sec period across Europe. Misfit is calculated from the corresponding smooth group speed maps inverted from the ambient noise and earthquake data, respectively. The standard deviation is indicated at the top left in each panel.